Surgical Microgrippers and Their Applications in a Dynamic Environment

By
Hyun Soo Yoon

A thesis submitted to Johns Hopkins University in conformity with the requirements for the degree of Master of Science in Engineering

Baltimore, Maryland
May 2016

© 2016 Hyun Soo Yoon
All Rights Reserved

Abstract

Minimally invasive surgery has improved medicine by reducing patient trauma, limiting scars, and accelerating recovery time. As the result of advancements in micro and nanotechnology, submillimeter star shaped devices known as microgrippers have been developed to enhance current minimally invasive procedures. The grippers are composed of metallic panels and a polymeric trigger layer, which allow them to respond to an external field and actuate at the body temperature. Most importantly, since they derive mechanical energy from the residual stress in the thin films, they are able to wirelessly grasp onto materials.

Although microgrippers have been exploited in several biopsies, they have yet to perform surgical tasks. To be utilized in surgeries, they must be able to travel through thin blood vessels, resist the pulsating blood flow, and avoid the trillions of blood cells. Manipulating the microgrippers with such precision requires a significant amount of force, but we discovered that the grippers had relatively weak magnetization. Therefore, we optimized the magnetic properties of the microgrippers by replacing the nickel panels with cobalt.

By electroplating cobalt, we advanced the microgrippers from weak magnets to strong, permanent magnets. The modification of the panels substantially increased the residual magnetization, saturation magnetization, and coercive force. With improved magnetic qualities, the microgrippers may revolutionize medicine through its novel applications in noninvasive surgery and targeted drug delivery.

Acknowledgements

First, I would like to thank my parents for their constant love and support; they sacrificed more than enough to provide me with education and other privileges. They inspire me to succeed and I am blessed to have such devoted parents. I would also like to thank my older brother, Richard, for his frequent checkups and motivations. His caring and protective nature made me strive to become a better person. Without my family, I would not have been able to achieve such a milestone in my life.

Next, I would like to thank Dr. David Gracias for introducing me to the world of micro/ nanotechnology. His outstanding portfolio and knowledge encouraged me to pursue my career in this specialized field. I would also like to thank Dr. Honggang Cui for directing my path throughout my undergraduate studies and offering treasured advices for the future. Without the guidance of my advisors, the course of my college life and future may have been drastically different.

I would like to thank past postdoctoral researcher Dr. Evin Gultepe and PhD candidate Qianru Jin for mentoring me throughout my undergraduate research and teaching me valuable microfabrication techniques. I would like to thank PhD candidates ChangKyu Yoon and Hye Rin Kwag for helping me adjust to the Gracias Lab and gladly providing assistance. I would like to thank postdoctoral researcher Dr. Arijit Ghosh for instilling knowledge on magnetism and collaborating with the University of Twente and I. Lastly, I would like to thank PhD candidate Danru Qu from the Chien Lab for the hysteresis measurements.

Table of Contents

List of Figures

List of Tables

Chapter 1: Introduction

1.1 Minimally Invasive Surgery

Surgeries are invasive by nature; most operations require large incisions that leave painful wounds and take months to fully heal. In 1987, Dr. Philippe Mouret revolutionized medicine by performing the first minimally invasive surgery in France [1]. Instead of removing a gall bladder through a 20 cm incision used in a traditional open cholecystectomy, he removed it through several small incisions. The following year, Dr. Barry McKernan performed the procedure in the United States with four 10 mm incisions, and ultimately popularized minimally invasive surgery [2]. **Figure 1** shows the procedures of a laparoscopic cholecystectomy vs open cholecystectomy.

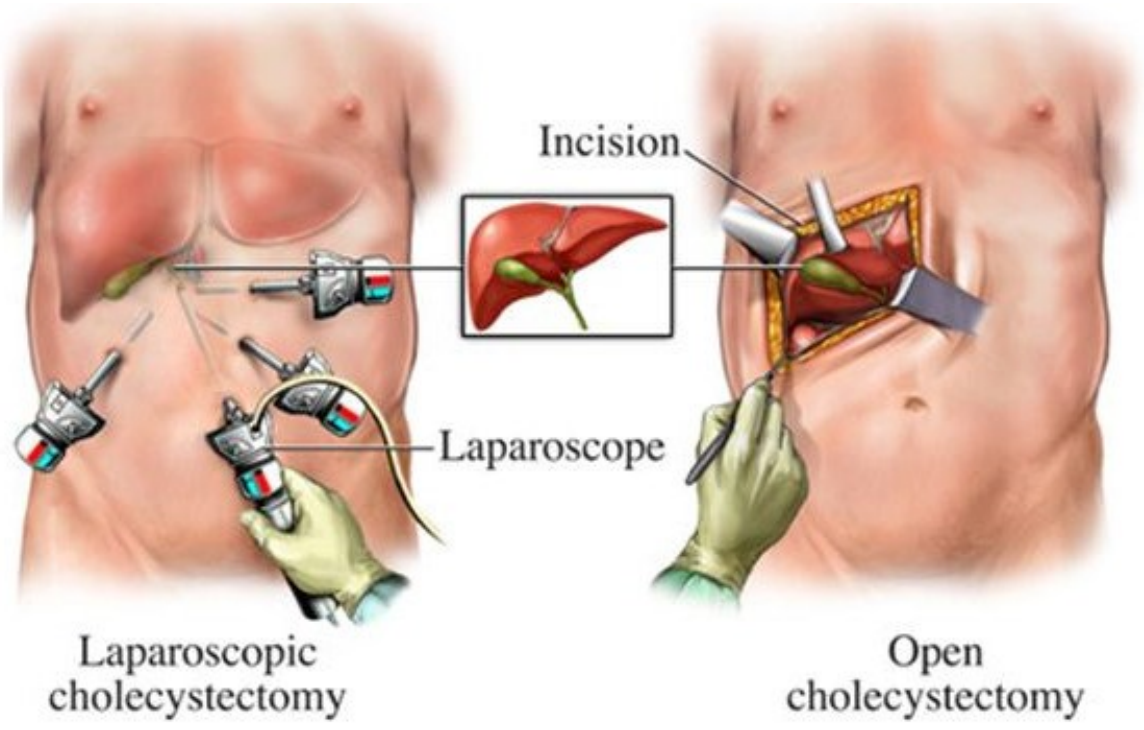

Figure 1: Laparoscopic Cholecystectomy vs Open Cholecystectomy. Laparoscopic surgeries require minimal incisions. Copyright © 2012 Drugline.org. All rights reserved. Image reprinted from ref [3]

Minimally invasive surgery refers to advanced surgical techniques that minimize the size of incisions and damage done to tissues to reduce postoperative pain, recovery time, and the risk of infection [1]. Minimally invasive surgery has replaced open surgery in most abdominal operations and the majority of cholecystectomies in the U.S are done laparoscopically [4].

1.1.1 Laparoscopic Surgery

In a laparoscopic surgery, several small incisions of about half an inch are usually made in the abdomen [5]. Often times, a cannula is used to insufflate the abdomen with carbon dioxide to create working space between the internal organs and the abdominal wall [1]. Trocars are then used to introduce a laparoscope, a light source, and various surgical tools into the body through the incisions or natural orifices [5]. The camera with the light source provides a magnified view of the surgical site on the operating monitor while the trocars act as portals to insert tools into the patient's body. **Figure 2** shows common surgical tools used in a laparoscopic surgery.

Figure 2: Common Instruments used in Laparoscopic Surgery.
Graspers, scissors, and needle holders are widely used in laparoscopic surgeries.
Copyright © 2016 Medical Equipment. All rights reserved. Image reprinted from Ref. [6]

Laparoscopic surgeries are often challenging due to the surgeon's loss of: tactile feedback, 3D visibility, wrist degrees of freedom, and a comfortable operating posture [7]. Therefore, robotic surgery was developed in 2000 by Intuitive Surgical (da Vinci Surgical System) to overcome the restrictions of previous minimally invasive procedures [7].

1.1.2 Robotic Surgery

Robotic Surgery is performed similarly to laparoscopic surgery but instead of operating directly on patients, the surgeon operates through a robotic surgical system with mechanical arms [7]. The robot translates the surgeon's hand motions into smaller movements for enhanced flexibility, precision, and control [7]. Furthermore, the console allows surgeons to see a high definition, magnified, 3D view of the surgical site while seated [8]. **Figure 3** shows robotic surgery in action.

Figure 3: Robotic Surgery. Patient is operated via da Vinci Surgical System. Copyright © 2015 Intuitive Surgical, Inc. All rights reserved. Image reprinted from Ref. [9]

Although minimally invasive surgeries have distinct advantages over open surgeries in patients' health and outcome, there are two major drawbacks with these techniques: the prolonged learning curve for surgeons and increased costs [10]. Due to the minimal access of the patient's body, many complications arise even for an experienced surgeon. Therefore, surgeons must complete extensive training courses, simulators, web based videos, and mentoring systems [10]. Even so, the first 20 procedures of a new minimally invasive surgeon are of maximum risk [11].

Secondly, the investment in the equipment and training may not compensate for the shorter hospital stays in some regions of the world. Robotic surgery, in particular, has been criticized for its high price; da Vinci Surgical System cost about $2 million and the procedure ranges from $1,600 to $3,200 per patient [12]. Nevertheless, the pros of the minimally invasive surgery continue to outweigh the cons and more patients are opting to get treated using these novel techniques.

1.2 Circulatory System

The circulatory system is a vast network of organs and vessels that allows blood to circulate and transport nutrients, hormones, and gases to and from the cells in order to maintain homeostasis and fight off diseases [13]. An average adult pumps about 2,000 gallons of blood that travel roughly 12,000 miles every day [14]. In addition to blood, the circulatory system circulates lymph, which is a clear fluid that removes waste and unwanted material [13].

The circulatory system consists of the heart, blood vessels, and blood [15]. The heart is a muscular organ with four chambers that pumps blood through the circulatory

system [15]. The base of the heart connects to the major blood vessels of the body including the aorta, vena cava, pulmonary trunk, and pulmonary veins [15].

1.2.1 Blood Vessels

Blood vessels are pathways for blood to flow throughout the body. All blood vessels contain a hollow space called the lumen that is surrounded by a thin layer of flattened cells called the endothelium [16]. The endothelium and the wall of the vessels prevent blood clots from forming by restricting the blood cells to inside the vessels [15]. Three major types of blood vessels are arteries, veins, and capillaries [15].

Arteries carry oxygenated blood from the heart to the rest of the body. They are composed of elastic fibers, smooth muscle fibers, and collagenous fibers [16].The elastic arteries, which consist of the aorta, are the largest blood vessels and have a diameter of 25 mm [17]. Due to their composition of mostly elastic fibers, they can constrict and dilate in response to various stimuli and withstand the direct pressure from the heart [17]. The muscular arteries have a diameter of 6 mm and deliver blood to specific organs [16]. Lastly, arterioles have a diameter of 30 μm and regulate blood flow into the capillary beds [16].

Veins carry deoxygenated blood from the rest of the body to the heart. They have a diameter of 5 mm and also contain elastic, muscle, and collagenous fibers [16]. They hold approximately 70% of the total blood volume and face much lower blood pressure than arteries [16]. Lastly, capillaries are the thinnest and the most common blood vessels. They have a diameter of 9 μm and extend throughout every tissues in our body. They consist of only a thin layer of endothelium and aid in the exchange of gases, nutrients,

and waste substances between the blood and the tissues. **Figure 4** shows blood flow through the arteries and veins in our circulatory system.

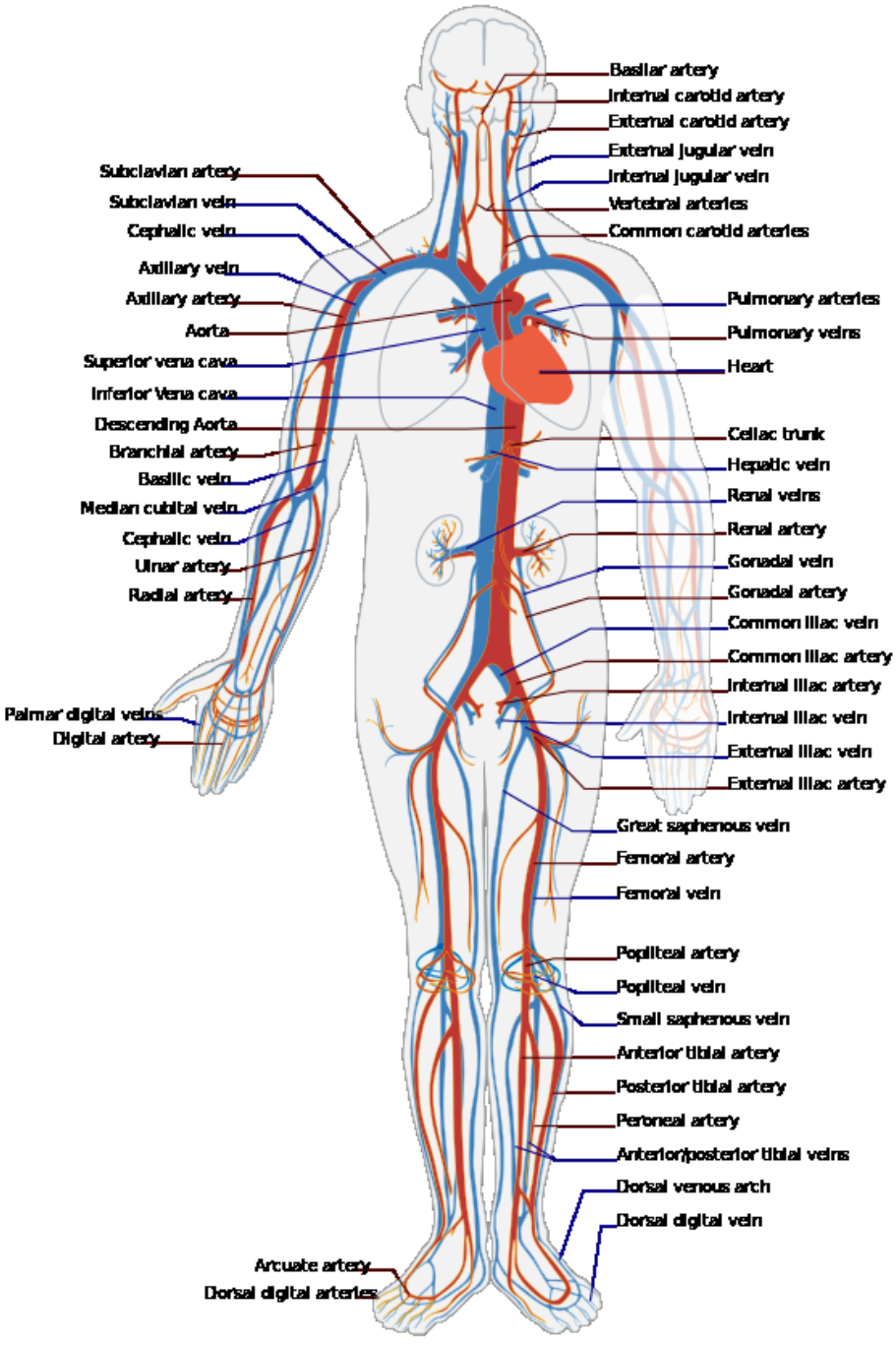

Figure 4: The Human Circulatory System. Red indicates arteries and blue indicates veins. Image reprinted with permission from Villarreal, Mariana. All Rights Reserved.

Blood pressure can vary depending on the blood vessel and is directly related to the blood flow by **equation 1**:

$$\text{Blood Flow} = \frac{\text{Blood Pressure}}{\text{TPR}} \qquad \text{[Equation 1]}$$

where blood flow is expressed as ml/min and blood pressure is expressed as mm Hg. Total peripheral resistance, TPR, is the measure of friction between the blood and the wall of the blood vessel, and is largely dependent on the viscosity of the blood, length of the blood vessel, and diameter of the blood vessel as shown in **equation 2** [16].

$$\text{TPR} = \mu * \frac{l}{r^4} \qquad \text{[Equation 2]}$$

where μ is the viscosity of the blood, l is the length, and r is the radius of the vessel. **Figure 5** shows the different characteristics of the blood vessels.

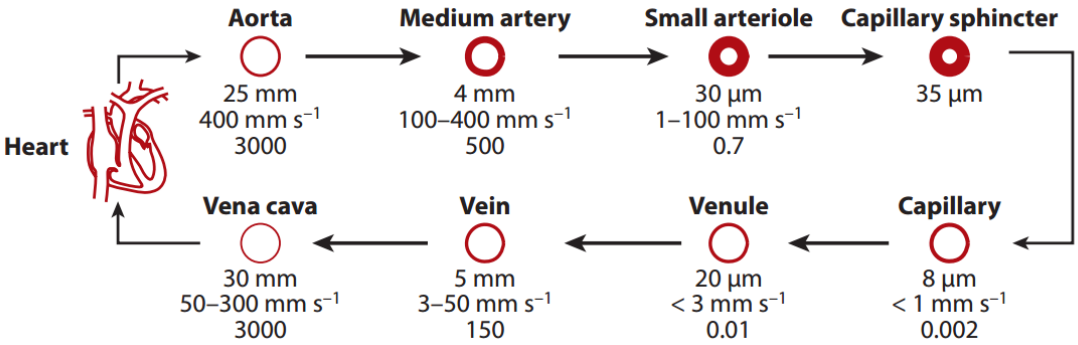

Figure 5: Characteristics of the Vessels in the Circulatory System. Displaying inner diameter, blood flow rate, and the Reynold's number. Blood pressure is the highest in the aorta and decreases throughout the circulatory system. Copyright © 2010, Annual Reviews. All rights reserved. Image reprinted with permission from Ref [59]

Systolic pressure and diastolic pressure are important measures in determining the average blood pressure [16]. Systolic pressure is the maximum pressure that occurs when the heart contracts and blood is forced into the aorta, while diastolic pressure is the minimum pressure that occurs in between heart beats at which blood is kept from flowing back into the heart [16]. Average blood pressure is determined through **equation 3**.

$$BP = DP + \frac{SP+DP}{3} \quad \text{[Equation 3]}$$

where BP is the average blood pressure, DP is the diastolic pressure, and SP is the systolic pressure.

1.2.2 Blood

Blood consists of plasma, red blood cells, white blood cells, and platelets [18]. Plasma makes up more than half of the blood's volume and is a mixture of mostly water but also dissolved salts and proteins such as antibodies and albumin [18]. It plays an important role in homeostasis, supplies water to, and absorbs excess water from tissues [18]. Red blood cells make up approximately 40% of the blood's volume and transport oxygen and carbon dioxide to and from other tissues [18]. They are 8 μm diameter biconcave disks that are mostly composed of a protein called hemoglobin that aids in the release and absorption of gases [18]. Their high surface area to volume ratio and flexibility allow them to fit into thin capillaries [18].

White blood cells make up less than 1% of the blood's volume but have crucial functions in the immune system such as breaking down bacteria and viruses and creating antibodies to defend against other infections [20]. The sizes of the spherical white blood

cells vary widely from as small as 7 µm in diameter in lymphocytes to as big as 25 µm in diameter in monocytes [21]. Lastly, platelets are small fragments of blood cells that help wounds heal by forming scabs and blood clots [22]. The components and the continuous flow of blood in our blood vessels make up the dynamic environment of our circulatory system. **Figure 6** shows the main components of blood.

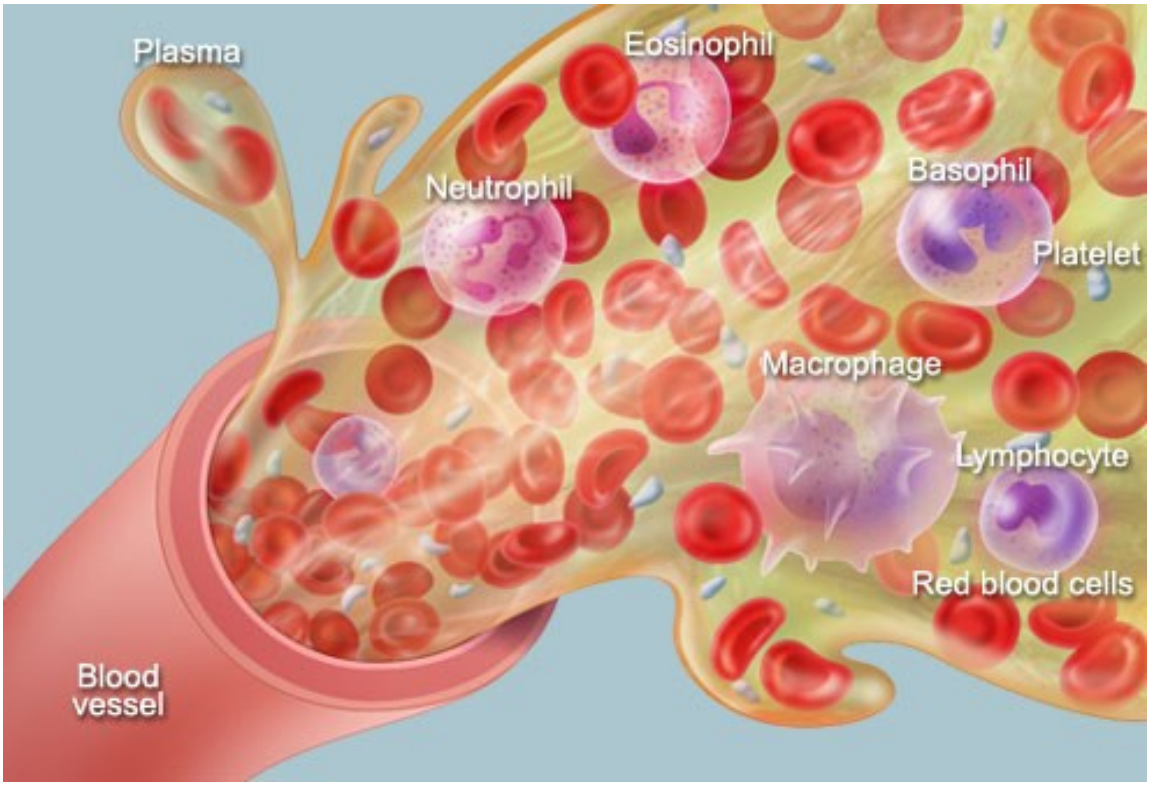

Figure 6: The Components of Blood. Plasma, red blood cells, white blood cells, and platelets constitute the blood. Copyright © 2014 WebMD. All rights reserved. Image reprinted from [23]

Chapter 2: Surgical Microgrippers

2.1 Background

Although minimally invasive surgery has drastically improved since it was first introduced, it has yet to advance into a completely noninvasive surgery. Noninvasive procedures such as radiation therapy can be used to shrink tumor and kill cancer cells, but the majority of non-cancer related operations require incisions to introduce trocars or other tethered tools into the body [25]. Without wires or tubes, surgeons have no mechanical control over their instruments and are unable to access and retrieve them from the patient's body [24].

The development of minimally invasive surgeries has motivated researchers to place a "miniaturized mechanical surgeon" inside a patient's body to perform surgery autonomously [26]. Removing the tethers from current methods of minimally invasive surgery will allow the surgeons to access hard to reach places in the body through narrow conduits such as the circulatory system or the reproductive system without harming nearby tissues [24]. Sub millimeter grasping devices known as microgrippers, which were inspired by the dicondylic joints of arthropods, have emerged as a viable and novel approach to noninvasive surgery [27].

Microgrippers were fabricated in 2009 for their biopsy purposes and demonstrated two distinct advantages over current methods [27]. First, they were able to be mass produced. The grippers were manufactured using standard microfabrication techniques; therefore, thousands of grippers were fabricated in parallel and in multiple substrates at a time [27]. By releasing a large number of microgrippers into the body, a slew of samples can be collected throughout the tissue for a more comprehensive biopsy screening.

Conventional biopsy techniques are unable to accomplish this feat due to a high risk of tissue damage and wound complications.

Secondly, microgrippers derive their mechanical energy from the residual stress in thin films, which eliminates the need for wires or tethers [27]. The release of stress in chromium drives the flexing of the bimetallic joints and ultimately folds the grippers [27]. As shown in **Figure 7**, Leung et al. theoretically and later experimentally found that a bilayer of 50 nm chromium and 200-250 nm copper resulted in approximately 90º folding angle depending on the elastic modulus of the polymer [27].

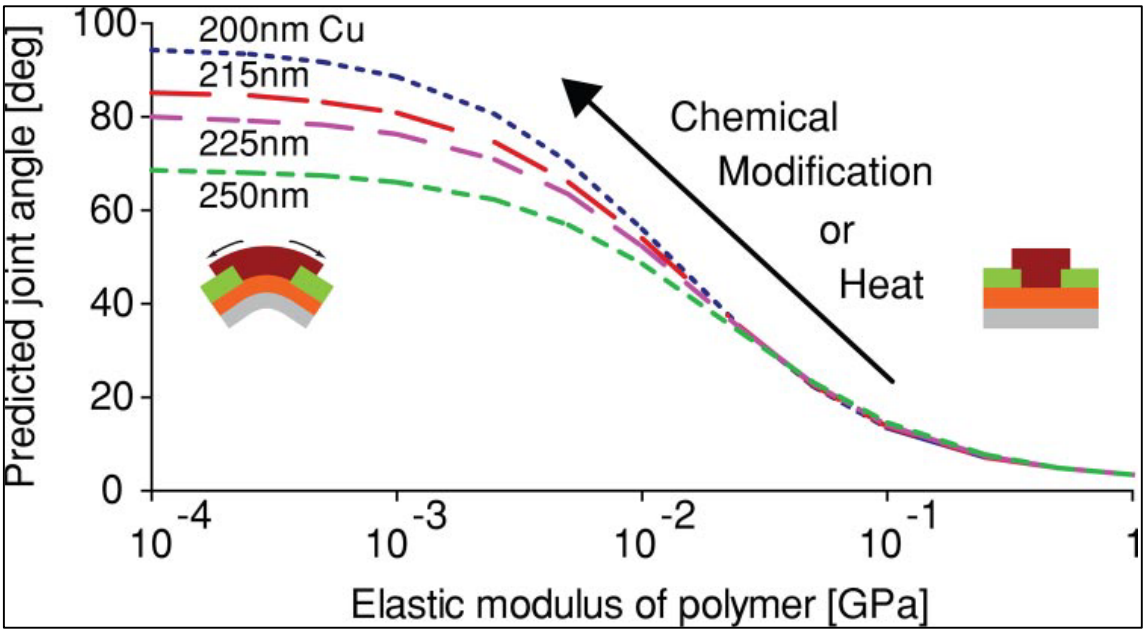

Figure 7: Stressed Bilayer Folding Angle Predictions. The relationship between the folding angle of the hinges and the Cr/Cu stress layer. Cr was kept constant at 50 nm while Cu varied from 200nm to 250nm. © 2009 PNAS. Image reprinted with permission from Ref [27].

Furthermore, the addition of electroplated nickel as phalanges and Cresol novolak resin-based photoresist as a trigger layer provided the grippers with unique properties [27]. The deposition of 6 μm nickel equipped the grippers with magnetic properties, while the deposition of photoresist prevented the grippers from immediately closing upon

release from the substrate. Instead, the polymeric trigger layer kept the grippers flat until heated to 40ºC, at which the stress in the bilayer overcame the resistance of the softened polymeric trigger layer and actuated the grippers [27].

As shown in **Figure 8ab**, microgrippers' mass production and unique properties allow them to fold simultaneously once they reach the appropriate temperature. **Figure 8c** shows the gripper's ability to maneuver through a coiled tube using the magnetic field and **Figure 8d-i** highlights the gripper's ability to navigate towards and capture a 275 µm bead upon reaching ≈ 40º C.

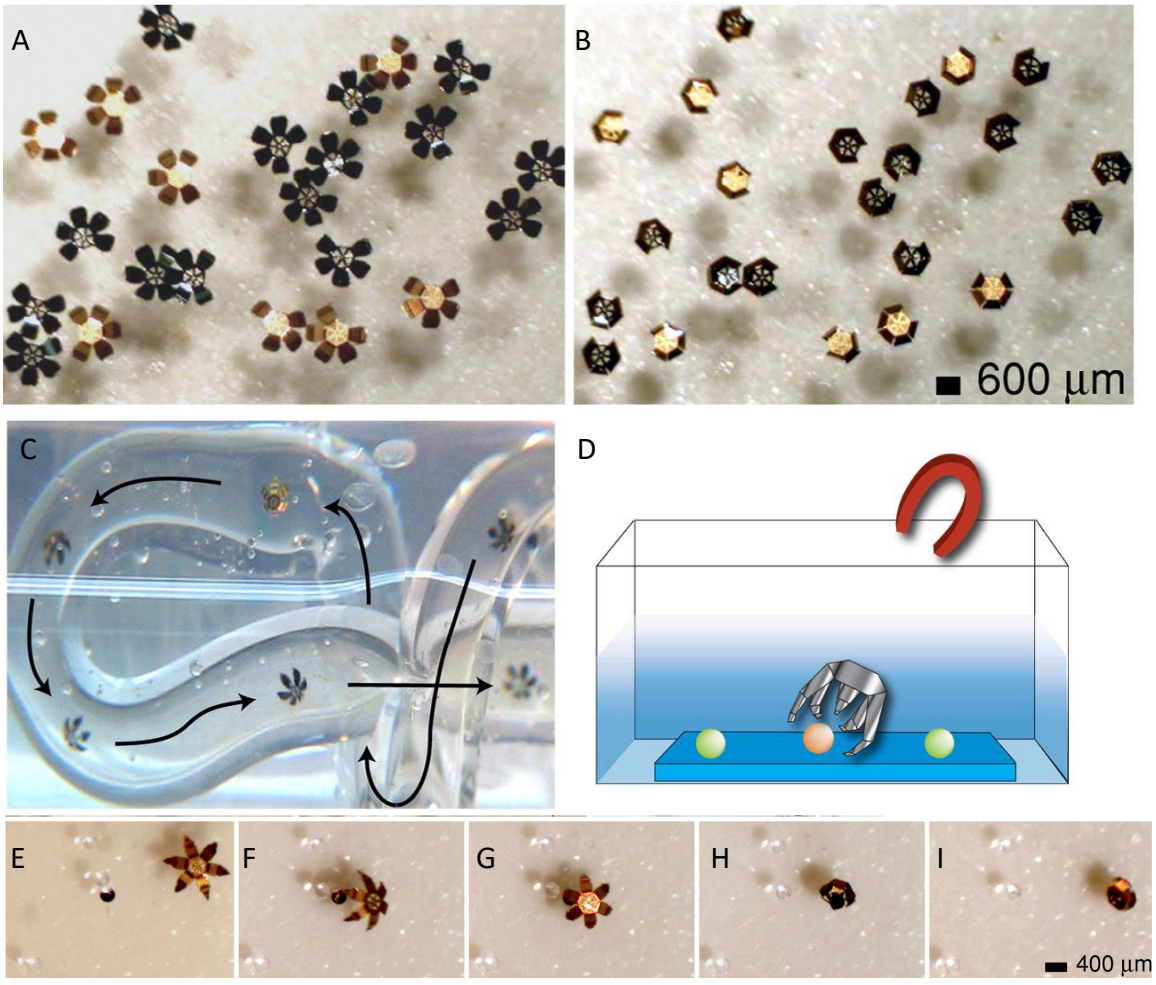

Figure 8: Untethered, Thermally Actuated, Magnetic Microgrippers. (a,b) Grippers fold en masse upon heating (c) Manipulation of the gripper through a coiled tube (d) A schematic of a microgripper capturing a bead (e-i) A microgripper capturing a 275 µm bead using a permanent magnet. © 2009 PNAS. Image reprinted with permission from Ref [27].

Metallic microgrippers were also successful in retrieving cells and tissue samples in vitro. Leung et al. guided a microgripper through a 1.5 mm diameter capillary tube using a magnet to capture clusters of live L929 fibroblast cells [27]. The microgripper remained flat until it reached the end of the tube at which the aqueous environment was heated to ≈ 40º C. Upon heating, the microgripper excised a portion of the cell mass stained with Neutral red and guided out of the capillary tube through a magnetic field. Leung et al. then checked for cell viability by placing the gripper with captured cells in the media and incubating them for 72 hours [27]. They found that the cells were alive, which indicated that the materials used in the fabrication of microgrippers as well as the cleaving process were biocompatible.

Furthermore, Leung et al. guided a microgripper through a same dimension capillary tube to capture a portion of a bovine bladder [27]. In this experiment, the gripper was rotated in the axial direction using a magnet in order to cut through the connective tissue. These experiments proved that though the features of the grippers were in the order of micrometer, they were robust enough to perform several biopsies. **Figure 9a-f** shows the gripper's capability of retrieving clusters of cells and a bovine tissue sample in vitro.

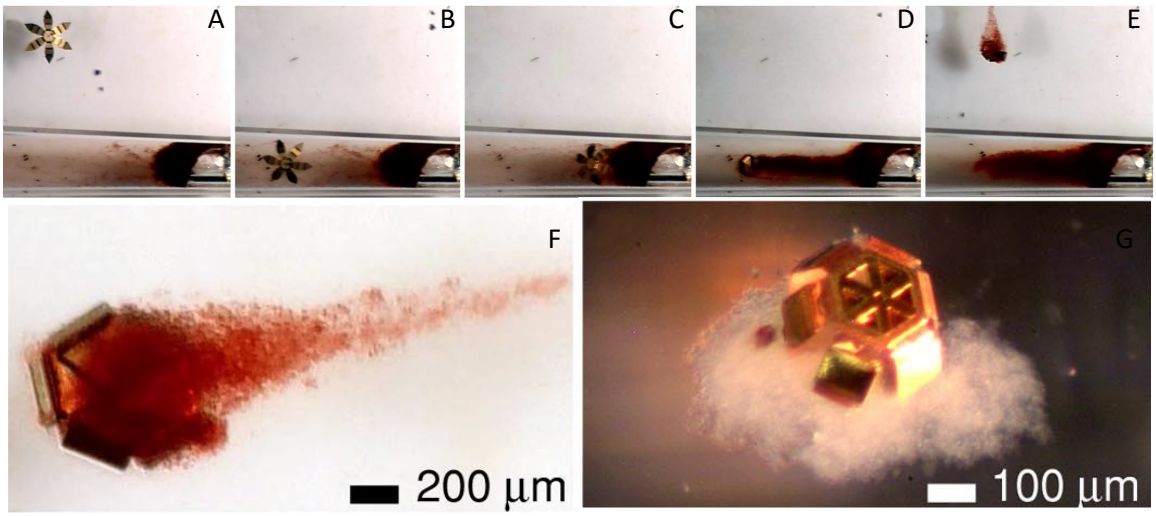

Figure 9: In Vitro Biopsies of Fibroblast Cells and Bovine Bladder Tissue. (a-f) Capture and retrieval of a cluster of fibroblast cells (j) Retrieval of a bovine bladder tissue. ©2009 PNAS. Image reprinted with permission from Ref [27].

More recently, 900 µm microgrippers were also successful in retrieving tissue samples. To demonstrate their ability to excise tissues from real organs, Gultepe et al. performed ex vivo biopsy using a porcine liver in a water bath [28]. Microgrippers were distributed over the bile duct opening using a pipette and within ten minutes the majority of the grippers grasped onto the tissue upon reaching the body temperature. The microgrippers along with their excised tissue sample were retrieved using a magnetic catheter. **Figure 10** shows the gripper's capability of retrieving a tissue sample ex vivo.

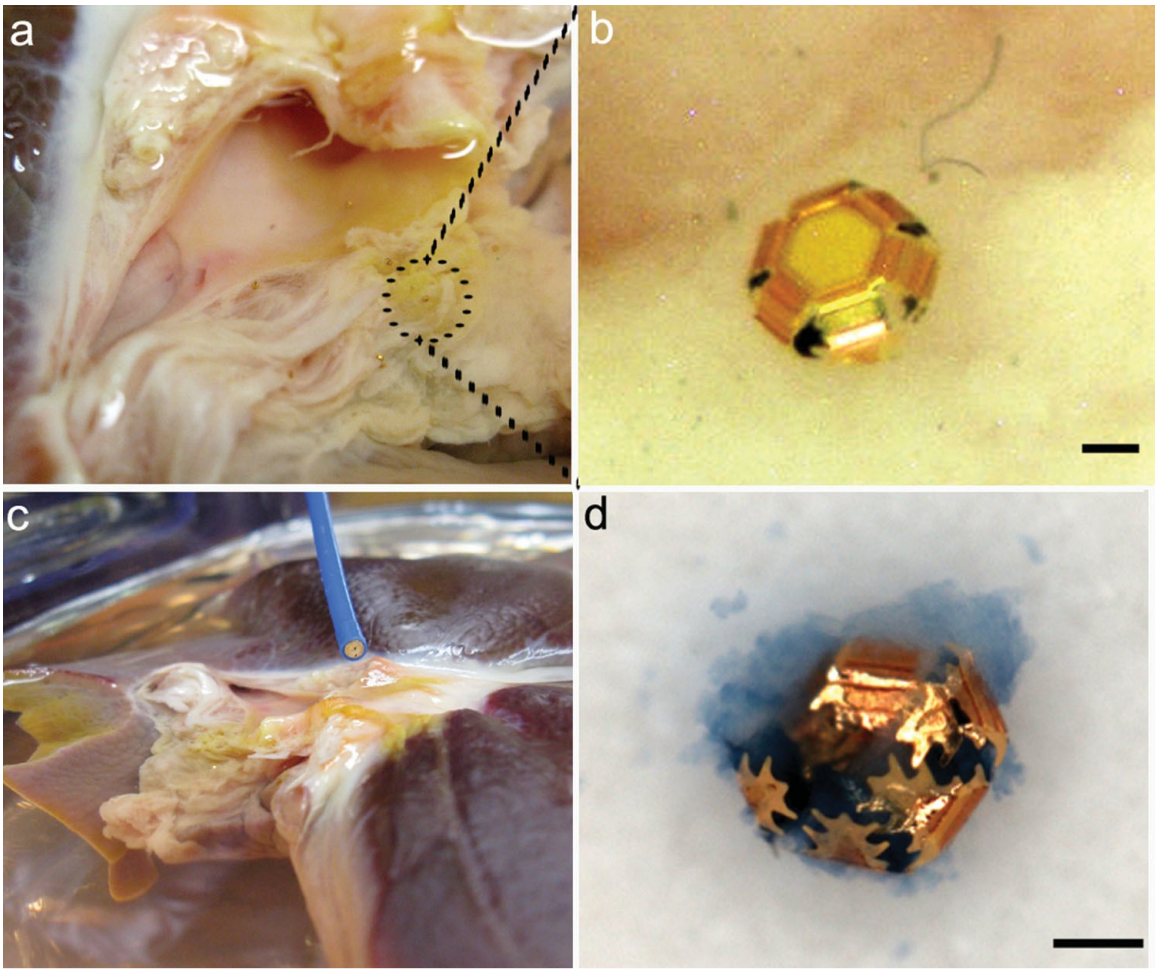

Figure 10: Ex Vivo Biopsy of a Porcine Liver. (a) Microgrippers distributed on the bile duct opening (b) Grasping of the tissue upon reaching body temperature (c) The retrieval of the gripper using a magnetic catheter (d) Excised tissue stained with trypan blue. © 2010 John Wiley and Sons. Image reprinted with permission from Ref [28]

Gultepe et al. also performed in vivo biopsy of a tissue within the biliary tree of a porcine model to show their ability to travel through natural orifices into hard to reach places of the body [28]. Endoscopic retrograde cholangiopancreatography (ERCP) endoscope was inserted into the mouth of the animal and into the duodenum [28]. Once the endoscope spotted the biliary opening, 1560 microgrippers were injected into the orifice through a deployment catheter [28]. After 10 minutes, the microgrippers reached the body temperature and began to close. The grippers along with their excised tissue sample were then retrieved through a deployment catheter which consisted of a magnetic

tip. Gultepe et al. visualized them optically by scraping off the samples from the grippers and staining them with trypan blue [28]. MRI screening showed that the average retrieval rates of the microgrippers were 95% [28]. **Figure 11** shows the grippers' ability to retrieve tissue samples in vivo.

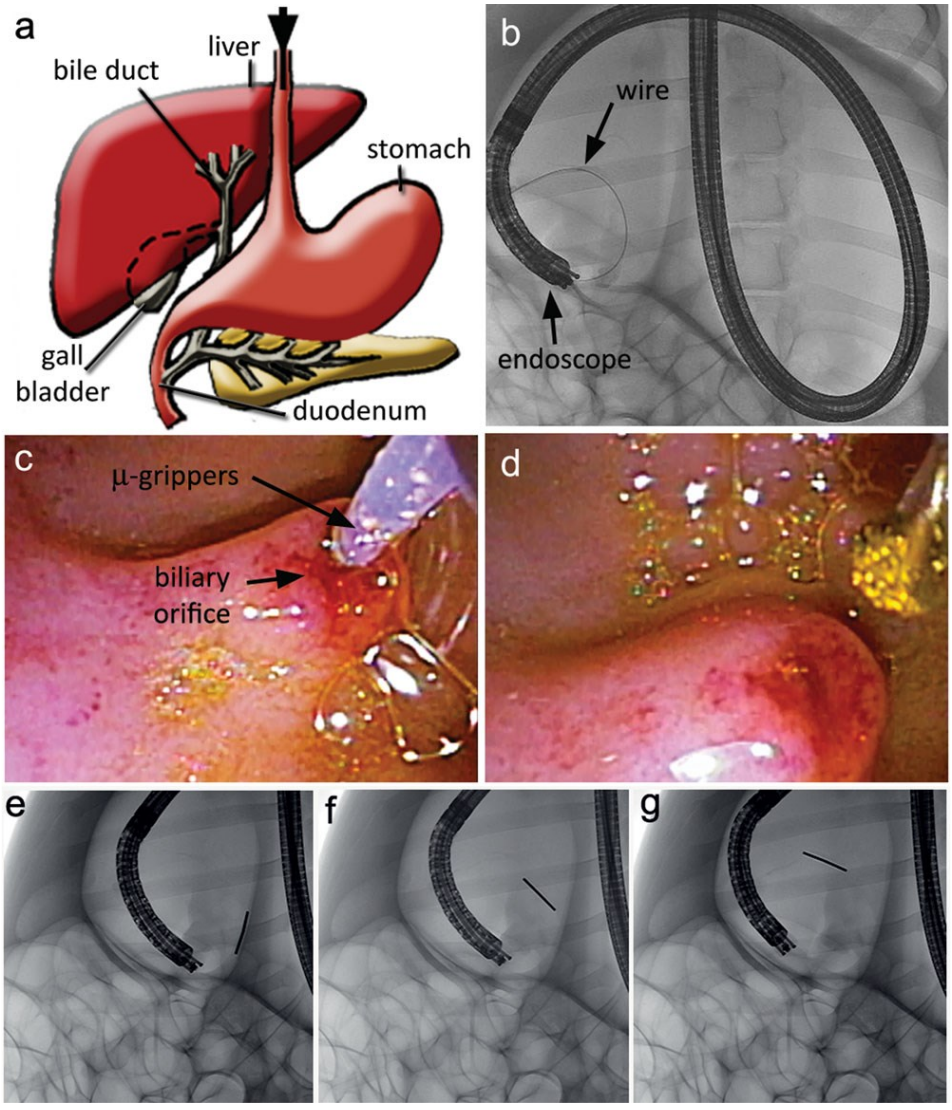

Figure 11: In Vivo Biopsy of the Porcine Bile Duct. (a) A schematic of the porcine gastrointestinal tract. Endoscope enters through the arrow depicted. (b) Fluorescent image of the endoscope entering the mouth. (c,d) The delivery and retrieval of the microgrippers using a catheter. (e-g) Fluorescent images of the catheter maneuvering inside the bile duct. © 2010 John Wiley and Sons. Image reprinted with permission from Ref [28]

Microgrippers have been successfully exploited for their use in biopsy; their parallel production and untethered actuation provide a more thorough yet less invasive screening. However, microgrippers have not been studied as extensively for their use in surgery. In order to be utilized as surgical tools, they must be able to fit into the thin blood vessels, withstand the blood pressure, and maneuver around the blood cells. Manipulating the grippers with such precision requires a substantial amount of magnetization. Therefore, we decided to optimize the microgrippers by modifying our rigid panels.

2.2 Microfabrication Techniques

The grippers were created using standard microfabrication techniques, which include repeated steps of photolithography, deposition, and etching. Photolithography is a process used to pattern geometric shapes from a mask onto the substrate [29]. In this step, UV light passes through the aligned mask onto the substrate coated with the photosensitive polymer, and alters the polymer's solubility in the developing solution [33]. Positive photoresists become soluble upon exposure while negative photoresists become insoluble upon exposure. After alignment and exposure, the substrate is developed in the solution to etch unwanted regions of the photoresist. **Figure 12** shows an overview of photolithography. [33]

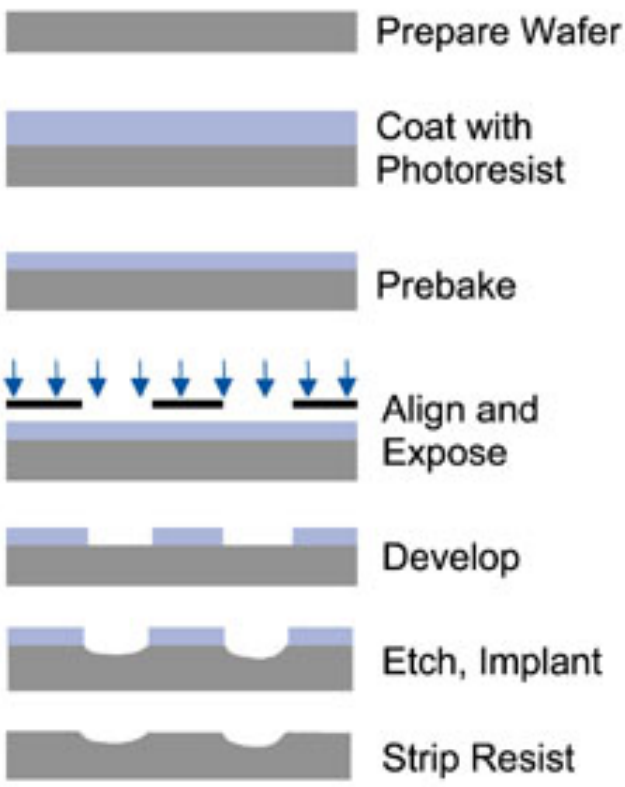

Figure 12: Overview of the Photolithography Process. Lithography with positive photoresist. © 2006 SPIE. Image reprinted with permission from Ref. [33]

After photolithography, thin film is deposited onto the resist coated substrate through chemical or physical deposition. Electroplating is a popular method of chemical deposition due to its relatively cheap cost and high deposition rates [31]. In this process, a current is applied to reduce metal cations from the electrolyte solution onto the cathode (substrate) [32]. At the same rate, metal atoms are oxidized at the anode (target metal) to continuously replenish the electrolyte solution with ions [32]. The factors that influence this process are current density, time, solution composition, pH, temperature, and agitation [34]. As shown in **equation 4**, the variables of electroplating are largely governed by Faraday's laws of electrolysis [35].

$$m = \left(\frac{Q}{F}\right) * \left(\frac{M}{z}\right) \qquad \text{[Equation 4]}$$

m is the mass of the substance liberated at an electrode, Q is the total electric charge passed through the substance, F is the Faraday's Constant, M is the molar mass, z is the valence of the metal [35].

Physical deposition includes thermal evaporation, which uses an electric filament to evaporate the target material onto the substrate. Since this process takes place in a high vacuum, the vapor particles travel directly from the tungsten boat onto the substrate, where they condense back to solid [36].

Lastly, etching is a process used to remove layers of material from the substrate [37]. In wet etching, the substrate is immersed in a bath of liquid etchant that diffuses into the material. The material becomes oxidized, dissolves in the solution, and forms a byproduct [38]. An example of wet etching is the developing step of photolithography, where a liquid etchant is used to remove regions of the photoresist.

In dry etching, the substrate is exposed to the plasma of an appropriate gas in a vacuum to remove material physically, chemically, or in combination [38]. In physical dry etching (sputtering), particles of high kinetic energy knock out and evaporate the atoms of the material from the surface [38]. In chemical dry etching, reactive ions form a compound with the atoms of the material and vaporize from the surface [38]. Lastly, dry etching can utilize both physical and chemical mechanisms, a process known as reactive-ion etching (RIE), to etch materials with high precision and efficiency [38].

Most of the fabrication takes place in the cleanroom, where the concentration of airborne particles is minimal through regulation in the temperature, humidity, pressure,

etc. [39]. This technology reduces any potential contamination and ensures high quality samples.

2.3 Fabrication of the Surgical Microgrippers

We adapted the designs of our microgrippers and the protocol for fabrication from Pandey et al. [40]. The grippers are 900 µm from tip to tip with 50 µm gaps in between the panels. Prior to the fabrication, we designed the photomasks for the stress layer, panel layer, and trigger layer using AutoCAD. **Figure 13** shows the masks that we used for the fabrication of the grippers.

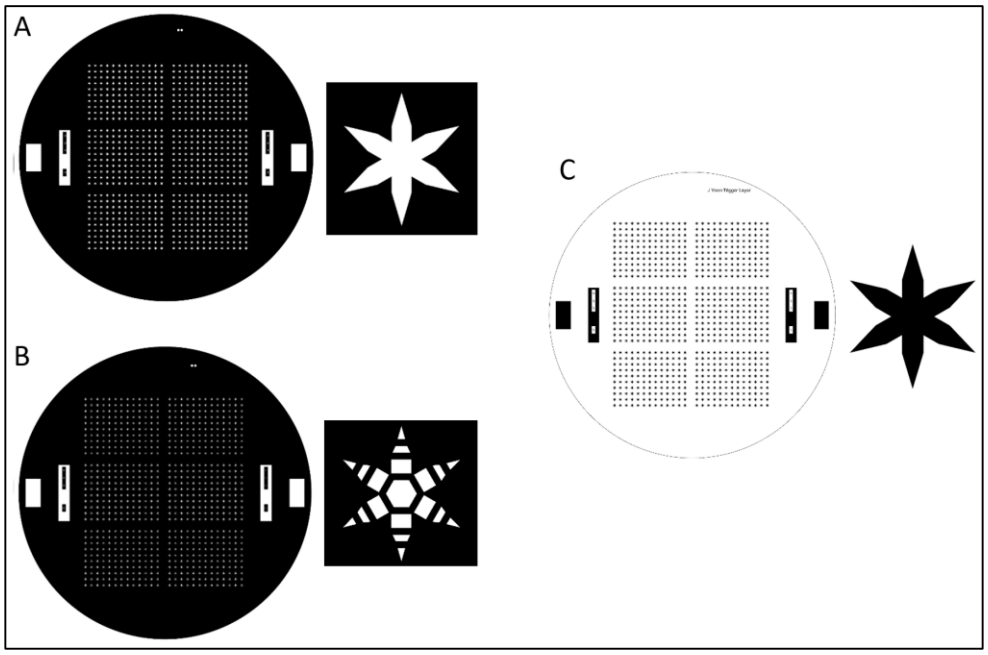

Figure 13: Photomasks for the Fabrication of Microgrippers. Grippers zoomed in to show details (a) Stress layer. 900 µm tip to tip (b) Panel layer. 50 µm hinge gaps. (c) Trigger layer

To begin fabrication, we cleaned eight 3 inch silicon wafers with acetone and isopropyl alcohol (IPA) then dried them with compressed air. We then deposited 15 nm chromium and 100 nm copper onto the wafers through thermal evaporation; chromium

serves as the adhesion layer between copper and silicon while copper serves as the sacrificial layer. We then spin coated positive photoresist Microposit SC-1827 onto the wafer at 3,000 rpm, to form 3 μm thick resist. We then baked the wafer at 115 ºC for one minute to evaporate the solvent and thicken the photoresist. We then aligned our wafer with our stress layer mask, exposed it at 180 mJ/cm^2 UV light, and developed it in a 5:1 ratio of deionized water and 351 Developer solution for 50 seconds. We then washed the wafers with deionized water and dried them with compressed air.

We then deposited 60 nm chromium and 100 nm gold onto the wafers through thermal evaporation; chromium serves as the stressed film while gold serves as the support layer. We then lift off the photoresist from the wafers in acetone and sonicated them to ensure complete removal of excess metal. After liftoff, we washed the wafers with IPA and dried them with compressed air to remove residues from the acetone. We then spin coated positive photoresist SPR-220 onto the wafer at 1,700 rpm, to form a 10 μm thick resist. We then baked the wafer at 60 ºC for 30 seconds, 115 ºC for 90 seconds, and 60 ºC for an additional 30 seconds. Next, we aligned our wafer with our panel layer mask, exposed it at 460 mJ/cm^2 UV light, and developed it in two separate baths of MF-26A for two minutes each. We then rinsed the wafers with deionized water and dried them with compressed air.

We then deposited 0.5 μm gold, 8.5 μm nickel, and an additional 0.5 μm gold through electroplating. The first layer of gold serves as an adhesion between thermally evaporated gold and electroplated nickel. The layer of nickel magnetizes the grippers and the second layer of gold prevents the nickel from etching in the subsequent steps. The combination of these layers form rigid panels that resemble the joints in our hand. We

then lift off the photoresist from the wafers in acetone, washed the wafers with IPA, and dried them with compressed air. We then spin coated a mixture of S1813 and S1805 photoresist, in a 1:5 volume ratio, onto the wafer at 1,800 rpm. We then baked the wafer at 115 ºC for 1 minute. Next, we aligned our wafer with our trigger layer mask, exposed it to 120 mJ/cm^2 UV light, and developed it in 5:1 ratio of deionized water and 351 Developer solution for 50 seconds. Lastly, we washed the wafers with deionized water and dried them with compressed air. **Figure 14** shows the schematics for the fabrication of microgrippers.

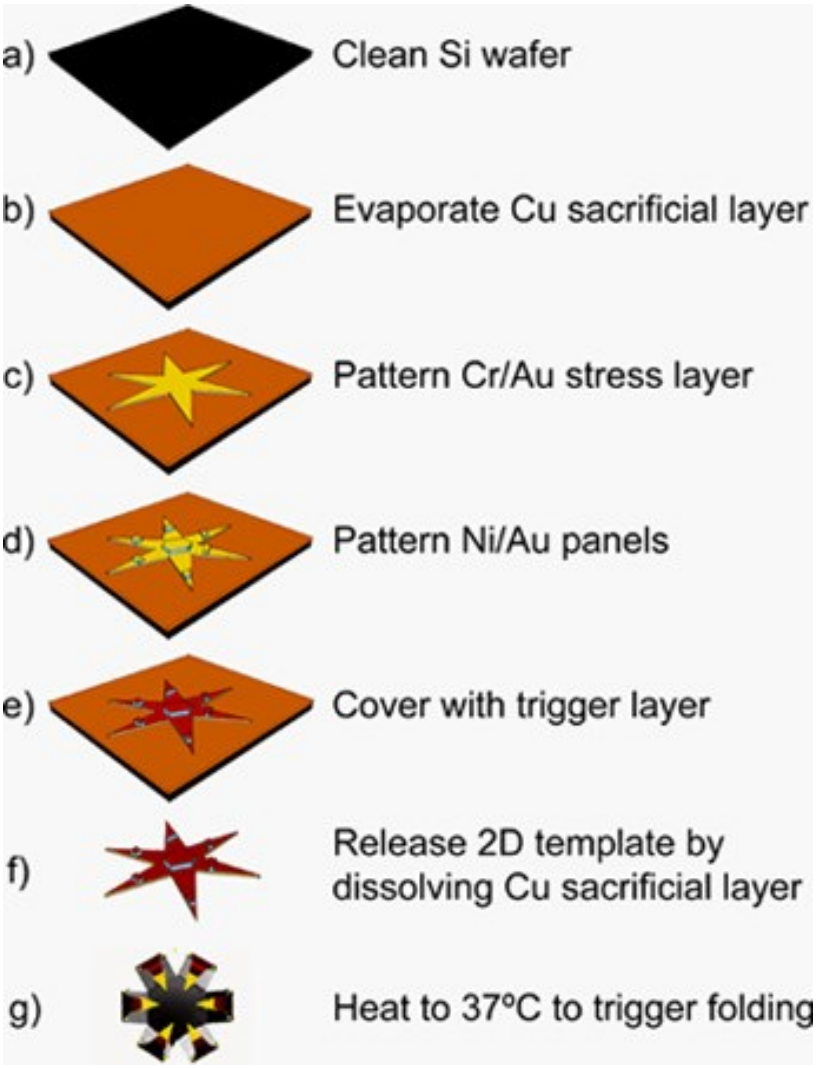

Figure 14: Schematics of the Fabrication of Microgrippers.
Copyright © 2012 Journal of Visualized Experiments. Image reprinted with permission from Ref. [40]

To actuate the microgrippers, we first cut the wafer into 6 pieces, each consisting of 130 grippers. We then immersed a single piece into Transene APS-100 in a glass petri dish to dissolve the copper sacrificial layer. Once the grippers separated from the wafer, we moved them into a dish of deionized water using a transfer pipette. Lastly, we slowly heat up the dish using a hot plate to close the microgrippers at 37 ºC. **Figure 15** shows the actuation of microgrippers in APS-100.

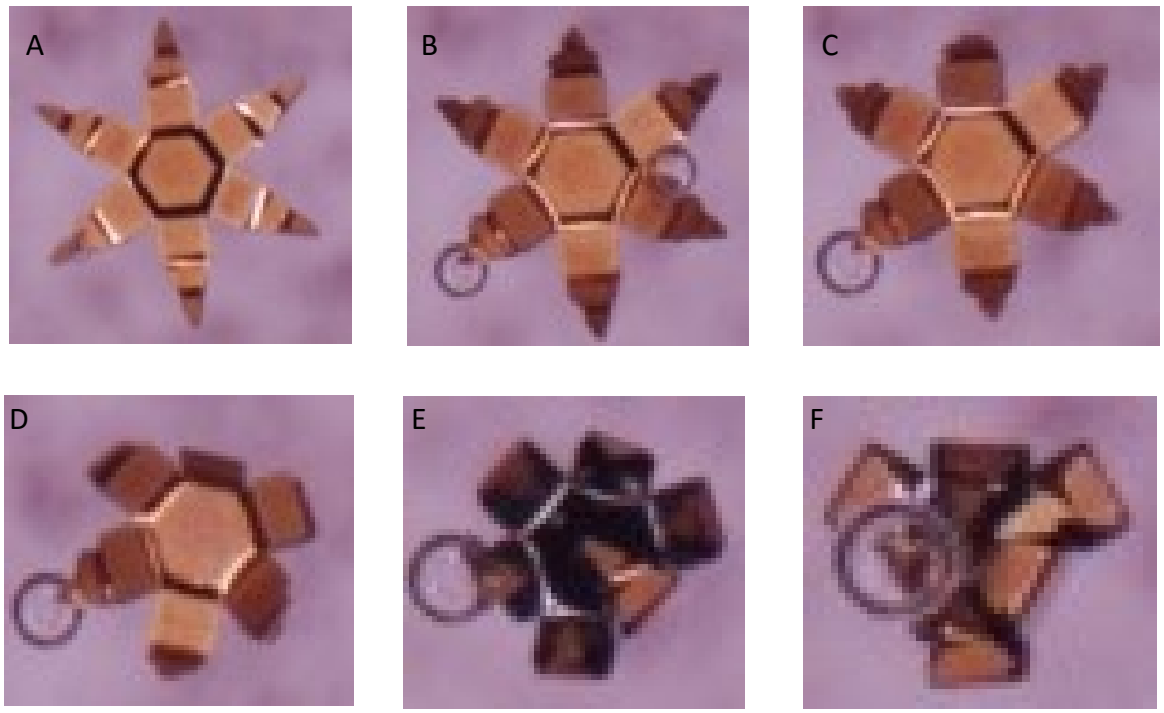

Figure 15: Thermal Actuation of Ni Microgripper. (a) 0 min / 29 ºC (b) 7 min / 32 ºC (c) 10 min / 35 ºC (d) 13 min / 37 ºC (e) 16 min / 39 ºC (f) 21 min / 40 ºC

Chapter 3. Optimization of the Magnetic Properties

3.1 Background

Our collaborators at the University of Twente Robotics Surgical Lab designed an experiment, which was inspired by the video game Pac-Man, to show the microgripper's potential as an autonomous surgical tool. The experiment consisted of a fluid reservoir and six orthogonally oriented electromagnets powered by a computer that plans the path and maneuvers the gripper through Proportional-Integral-Derivative (PID) controllers. **Figure 16** shows the setup of our experiment.

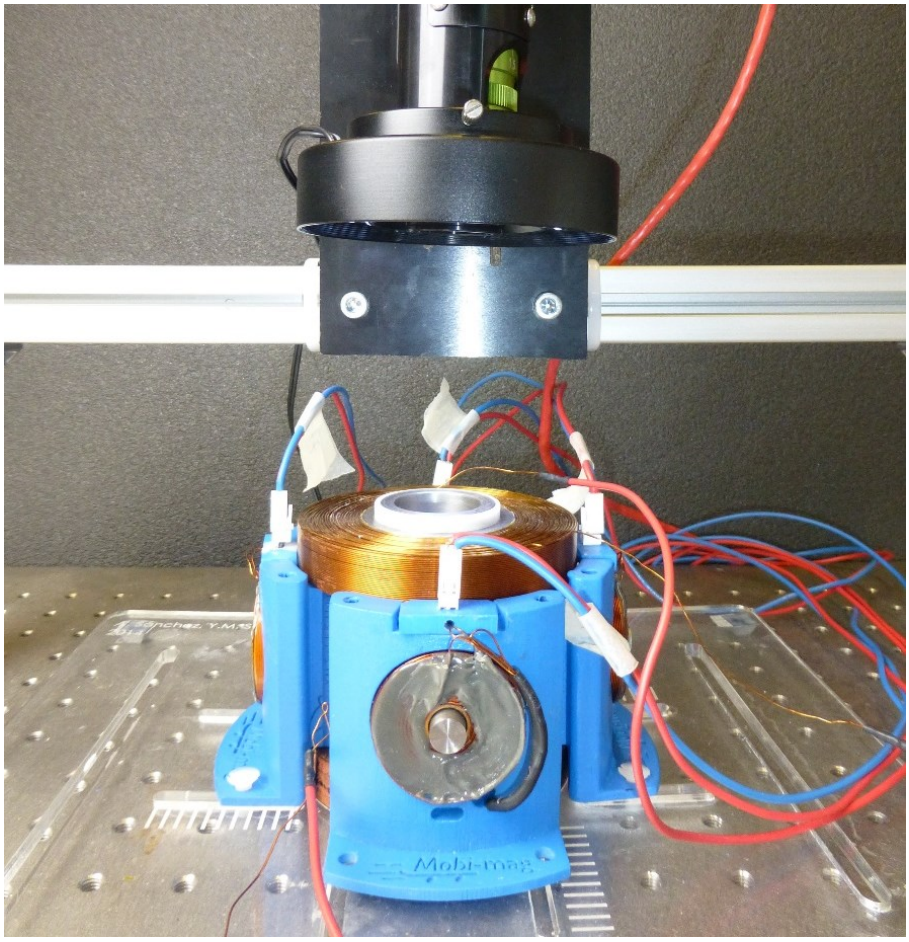

Figure 16: Pac-Man Experiment Setup. Image reprinted with permission from Ongaro, Federico.

We intended for these grippers to detect, grasp, and transport a target material to a specific region while avoiding obstacles. The target material was a tissue that contains a high concentration of low density lipoproteins while the obstacles were composed of both static and dynamic virtual objects.

During our experiment we discovered that the force between the grippers and the electromagnets were insufficient. At times, the force of static friction at the surface of the petri dish was strong enough to prevent the grippers from sliding. After unsuccessfully looking into treatments to reduce the friction at the surface, we decided it would be more feasible to maximize the interaction between the grippers and the applied field rather than minimizing the interaction between the grippers and the surface of the dish. Therefore, while our collaborators worked on increasing the magnetic field of their set up, we decided to improve the magnetization of the grippers by replacing nickel panels with cobalt.

3.2 Ferromagnetism

Ferromagnetism is the strongest class of magnetism and exists in some of the transition metals with unpaired electrons such as iron, cobalt, and nickel [41]. Ferromagnetic materials exhibit a long-range order of magnetic domains that individually act as elementary magnet with its own dipole moment [42]. As shown in **figure 17**, in the absence of an external magnetic field, these domains are randomly oriented, and the material is unmagnetized [42]. However, in the presence of an external field, the domains that are aligned in the direction of the field begin to grow at the expense of others, and the material becomes magnetized [42].

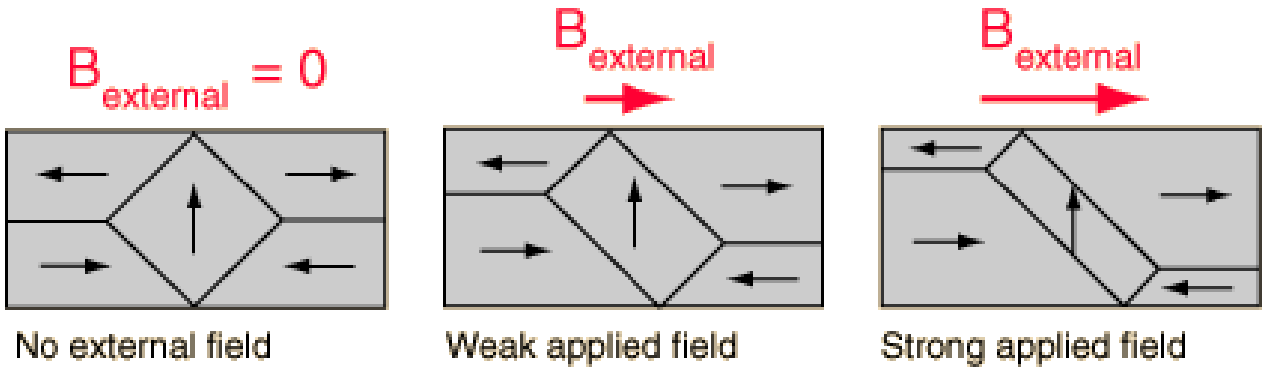

Figure 17: Magnetic Domains in Response to an External Field. Copyright © 2012 Hyperphysics. Image reprinted with permission from Ref. [42]

Due to their high permeability, ferromagnetic materials are easily magnetized and can reach saturation magnetization with enough applied field. At this limit, the material is almost entirely composed of a single domain aligned with the applied field, and the increase in the strength of the field has minimal effect on the magnetization of the material [42]. When the applied field is removed, the material still retains a fraction of the magnetization known as the residual magnetization or remanence, M_r [42].

In order to demagnetize the material, the applied field must be driven in the reverse direction until it reaches the coercive force or coercivity, H_c [43]. When an alternating magnetic field is applied until it reaches saturation magnetization, M_s, in both directions, a hysteresis loop can be generated by plotting the magnetization of the material as a function of the strength of the applied field [42]. The magnetization of the material can be determined using **equation 5**.

$$M = \frac{\mu_t}{V} \qquad \text{[Equation 5]}$$

Where M is the magnetization of the material, μ_t is the net magnetic dipole moments, and V is the total volume of the material.

As shown in **figure 18**, important magnetic properties of the material can be determined by tracing out the hysteresis loop.

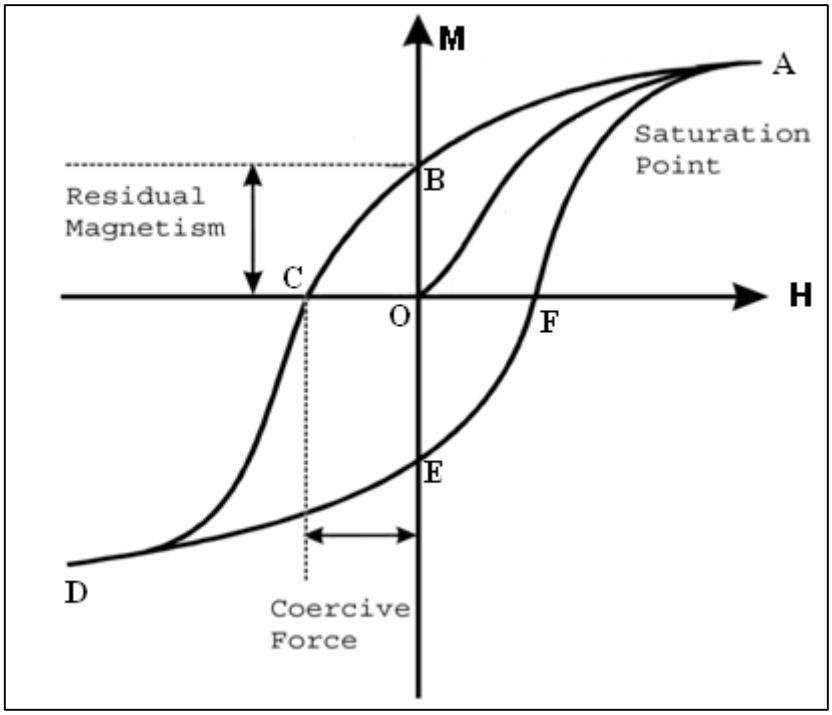

Figure 18: Hysteresis Loop of a Ferromagnetic Material. M_s, M_r, and H_c can be determined from the hysteresis Loop. Curve starts at the origin for an unmagnetized ferromagnetic material. Copyright © 2013 VLab. All rights reserved. Image reprinted from Ref. [47]

It is also common to measure the magnetic flux density or induction inside the material by using **equation 6**.

$$B = \mu_o(H + M) \qquad \text{[Equation 6]}$$

Where B is the magnetic flux density in T, μ_o is the permeability of free space ($1.25663706 \times 10^{-6}$ T*m/A), H is the applied field strength in A/m, and M is the magnetization in A/m

3.3 Cobalt vs Nickel

Cobalt and nickel are used extensively in the industries for not only their robust magnetic properties but also their physical and mechanical properties [48]. When compared in bulk, as shown in **Table 1**, cobalt has stronger magnetic properties than nickel [42] [45].

Table 1: Magnetic properties of bulk nickel and cobalt (annealed)

Magnetic Properties	Nickel	Cobalt
Saturation Induction, B_s (T)	.62	1.8
Residual Induction, B_r (T)	.40	.49
Coercive Force, H_c (A/m)	55.7	707
Relative Permeability, μ_r	110	68
Type of Magnet	Soft	Hard

Cobalt's saturation induction is almost three times greater than nickel's while cobalt's residual induction is 25% greater than nickel's. Furthermore, the coercive force of cobalt is 13 times greater than that of nickel. A low coercivity and residual induction are characteristics of a soft magnetic material while a high coercivity and residual induction are characteristics of a hard magnetic material [42].

One advantage that nickel has over cobalt is its higher relative permeability, which is the defined by **equation 7**.

$$\mu_r = \frac{\mu}{\mu_o} \qquad \text{[Equation 7]}$$

Where μ_r is the relative permeability, μ is the permeability of the material, and μ_o is the permeability of free space.

Nickel's higher relative permeability indicates that its magnetization and magnetic flux density have an expeditious response to an increase in the external field and will reach saturation earlier than cobalt.

3.3.1 Cobalt vs Nickel in MEMS

Both soft and hard magnetic materials are used in MEMS due to their low mass, low power consumption, and reliability [46]. Soft magnetic materials such as permalloy (81% iron and 19% nickel) and nickel are most commonly used [46]. Their high magnetic saturation, low coercivity, and corrosion resistance make them suitable in the development of MEMS [46].

On the contrary, hard magnetic materials are rarely used in MEMS due to the lack of available deposition and micromachining processes [46]. Cobalt alloys are most commonly used amongst the hard magnetic materials because of their highly anisotropic (HCP) structure [46]. The elements that form an alloy with cobalt tend to concentrate at the grain boundaries and surround the cobalt. This structure increases the energy barrier to realign the magnetic domains and forms a permanent magnet with high coercivity [46]. Furthermore, Myung et al. found that electrodeposited cobalt alloys have promising magnetic properties such as high remanence and saturation magnetization [46]. As shown in **figure 19**, cobalt alloys have stronger overall magnetization than nickel [46].

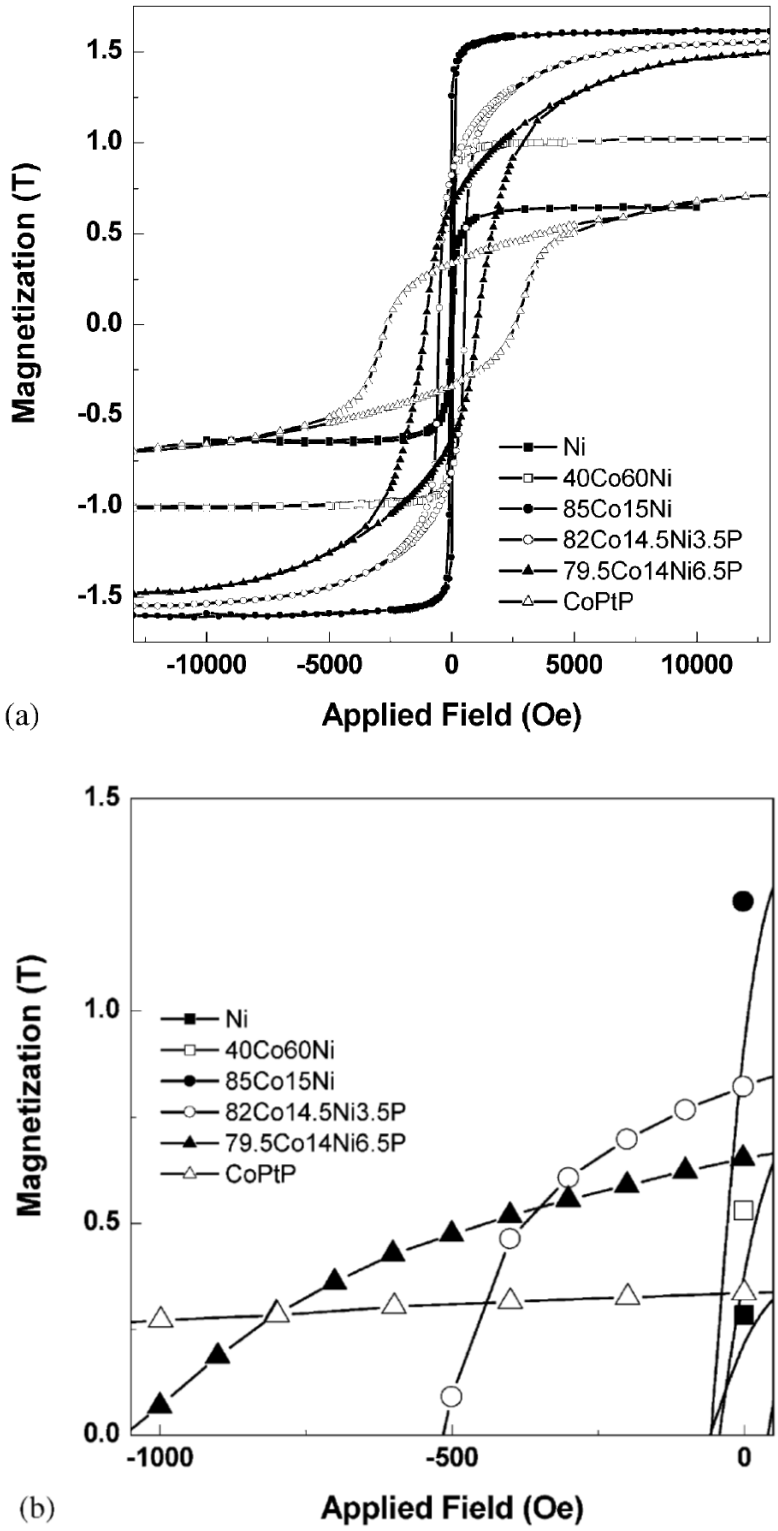

Figure 19: Magnetism of Cobalt Alloys vs Nickel in MEMS. Comparison of Ms, Mr, and Hc in the (a) Hysteresis loop (b) B-H curve for cobalt alloys and nickel. © 2003 JMMM. Image reprinted with permission from Ref [46]

Although nickel and other soft magnetic materials are used more extensively in MEMS, for devices that require stronger magnetic qualities, cobalt and its alloys may be more suitable. Therefore, we decided to electroplate cobalt in place of nickel to obtain a higher remanence and saturation magnetization.

3.4 Experimental Methods

3.4.1 Characterization of Electroplated Nickel

Prior to optimizing the grippers, we analyzed the magnetic properties by tracing out the hysteresis loop. We placed four grippers in the GMW Associates 250 mm VSM and measured their net dipole moment against the field. We then calculated the magnetization of the grippers using equation 5. Due to the magnetic anisotropy of ferromagnetic materials, we measured their moments in plane and out of plane field. **Figure 20** shows the hysteresis loops of the microgripper with nickel panels.

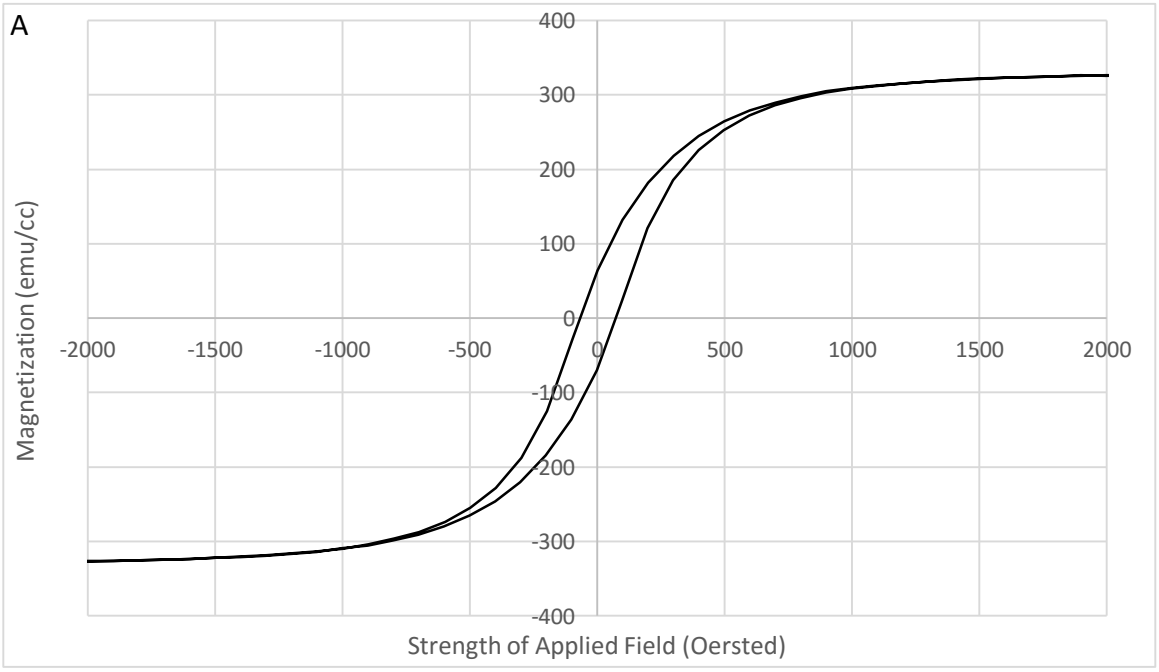

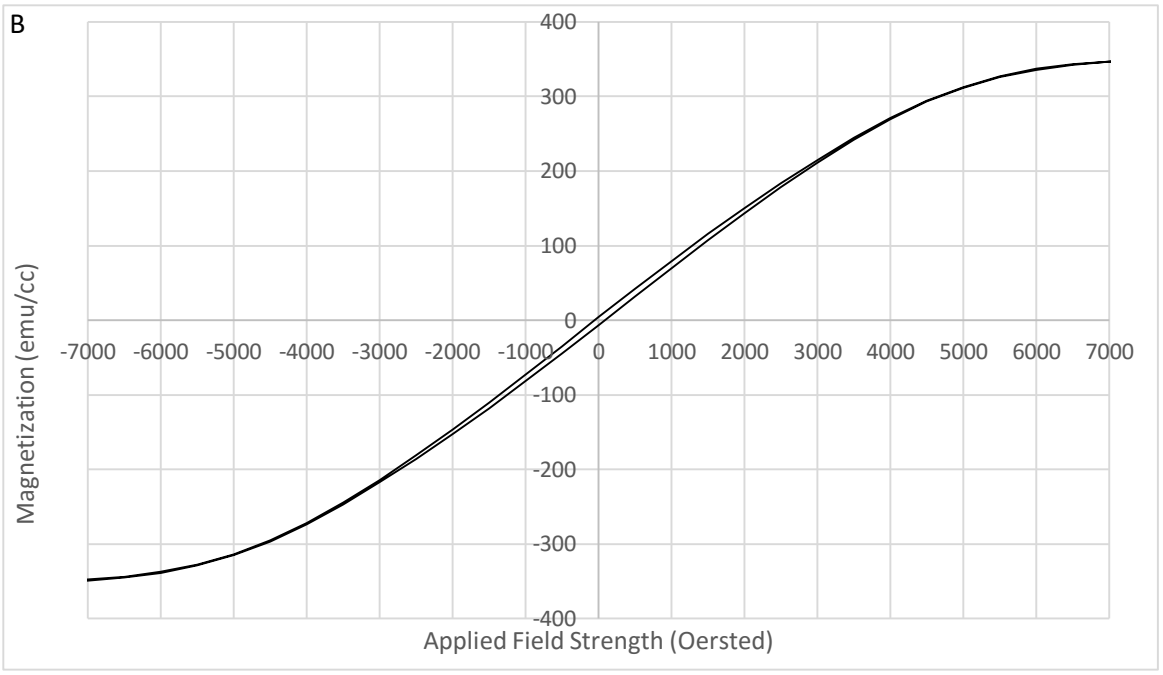

Figure 20: Hysteresis Loops of Ni Microgrippers. (a) In plane field (b) out of plane field. Grippers have near the same Ms in both fields.

From **figure 20**, we confirmed the preferred orientation of the crystallites in electroplated, ferromagnetic thin films. It is energetically favorable to apply the magnetic field in the direction parallel to the plane rather than perpendicular because the latter increases demagnetization energy [51]. The behavior of a ferromagnetic material is governed by **equation 8**, which involves various types of magnetic energy that collectively make up the thermodynamic potential of a ferromagnetic crystal in thin film [51].

$$F = F_{exch} + F_{dem} + F_H + F_{anis} + F_\sigma \qquad \text{[Equation 8]}$$

Where F_{exch} is the exchange energy, F_{dem} is the demagnetization energy F_H is the

Zeeman energy, F_{anis} is the magnetocrystalline energy, and F_{σ} is the magnetoelastic energy.

The exchange energy favors the parallel orientation of the domains in a crystal and is responsible for the short-range interactions of nearby crystallites while the demagnetization energy favors the perpendicular orientation and is responsible for the long-range interactions [51]. Zeeman energy is the potential energy of the crystal, magnetocrystalline energy is the differential energy in the magnetizing directions, and magnetoelastic energy is the energy due to external and internal stress [51].

Although the gripper had the same magnetic saturation in both fields, perpendicular required a much stronger field due to the overwhelming demagnetization energy. Furthermore, the residual magnetization and coercive force significantly decreased when magnetized along the hard axis. Therefore, we decided to apply the field in parallel to the plane for subsequent measurements.

3.4.2 Electrodeposition of Cobalt Panels

To determine the variables for the electrodeposition of cobalt panels, we modified equation 4 or the Faraday's laws of electrolysis to solve for time and current. **Equations 9 and 10** solve for time and current respectively.

$$t = \frac{T}{J} * \frac{\rho n F}{A} \qquad \text{[Equation 9]}$$

Where t is the time in seconds, T is the thickness in m, J is the current density in A/cm^2, ρ is the density in g/cm^3, n is the valence, F is the Faraday's constant, and A is the molar mass in g/mol.

$$I = J * S \qquad \text{[Equation 10]}$$

Where I is current in A, J is current density in A/cm^2, and S is the surface area to be plated in cm^2.

Using **equations 9 and 10**, we designed four trials of cobalt deposition with varying current density as shown in **Table 2**.

Table 2: Variables for the electrodeposition of cobalt

Trial #	Current Density (mA/cm^2)	Current (mA)	Time (min)
1	10	12.9	41.3
2	20	25.8	20.6
3	30	38.7	13.8
4	40	51.6	10.3

Once we calculated the variables, we electroplated cobalt onto the panels using a simple sulfate solution ($CoSO_4 \cdot 7H_2O$ 0.89 mol/dm^3) at 50 ºC and pH 5 as demonstrated by Armyanov [51]. The solution at these settings ensured that the crystallographic structure of cobalt is single HCP phase.

There are two phases in electroplated Co coating that may exist simultaneously: hexagonal close-packed and face-centered cubic (FCC). The two structures have drastically different magnetic properties. HCP has one axis of easy magnetization while FCC has four; to avoid any bias due to the structure and composition of the metal, we decided to electroplate single HCP phase cobalt.

3.5 Results and Discussion

3.5.1 Film Quality of the Electroplated Cobalt

After electroplating cobalt, we took images of the grippers using Nikon AZ100 optical microscope. **Figure 21** shows the changes in the film quality as a response to increasing current density.

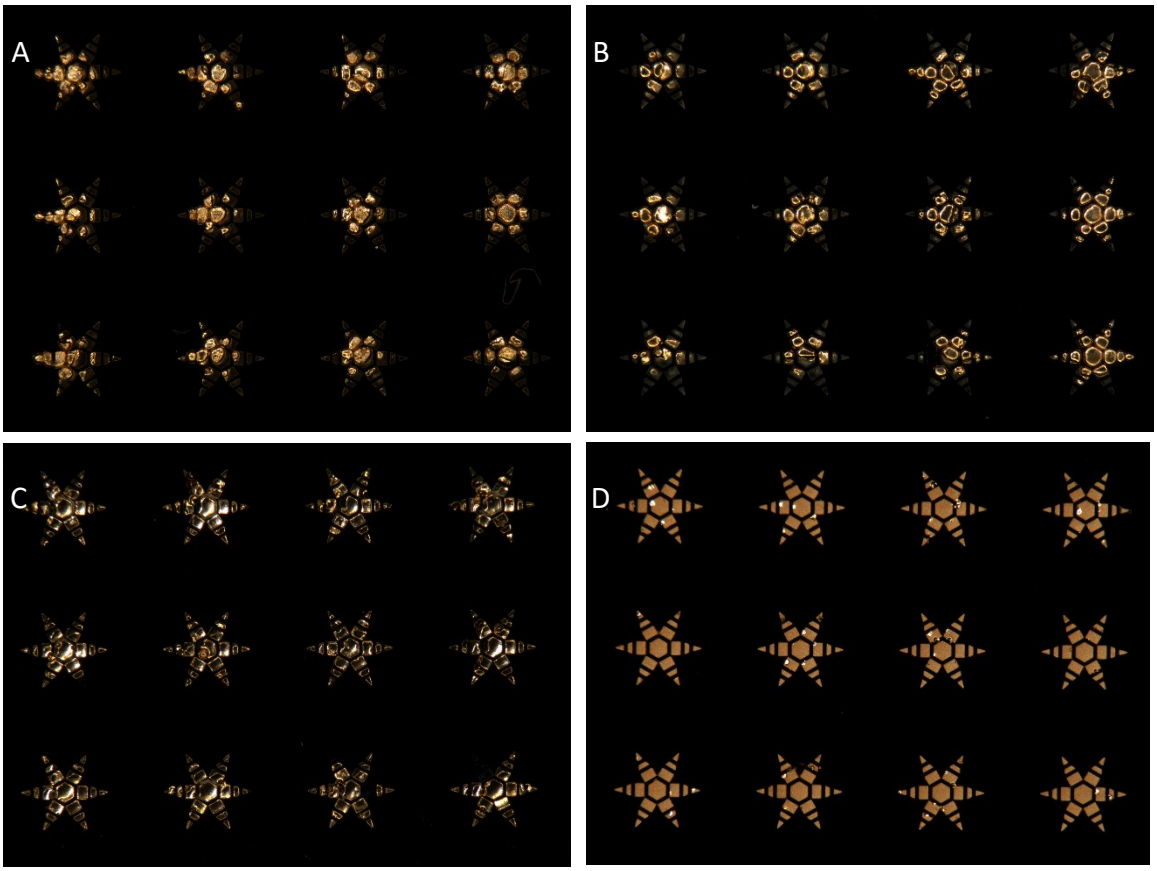

Figure 21: Effect of Current Density on Film Quality (Overview). Optical images of the microgrippers at varying current density (a) 10 mA/cm² (b) 20 mA/cm² (c) 30 mA/cm² (d) 40 mA/cm². Current Density of 40 mA/cm² produced highest Co film quality.

As shown in **figure 21**, the current density plays a key role in the film quality of the electroplated cobalt. At low current densities (10, 20, 30 mA/cm^2), the film quality is unsatisfactory due to an incomplete coating. Weak electric force between the particles and the surface, and slow nucleation rate lead to fractional deposition [55]. Furthermore, as shown in **figure 22**, we found that some of the grippers at lower current densities had a much thicker coating than others.

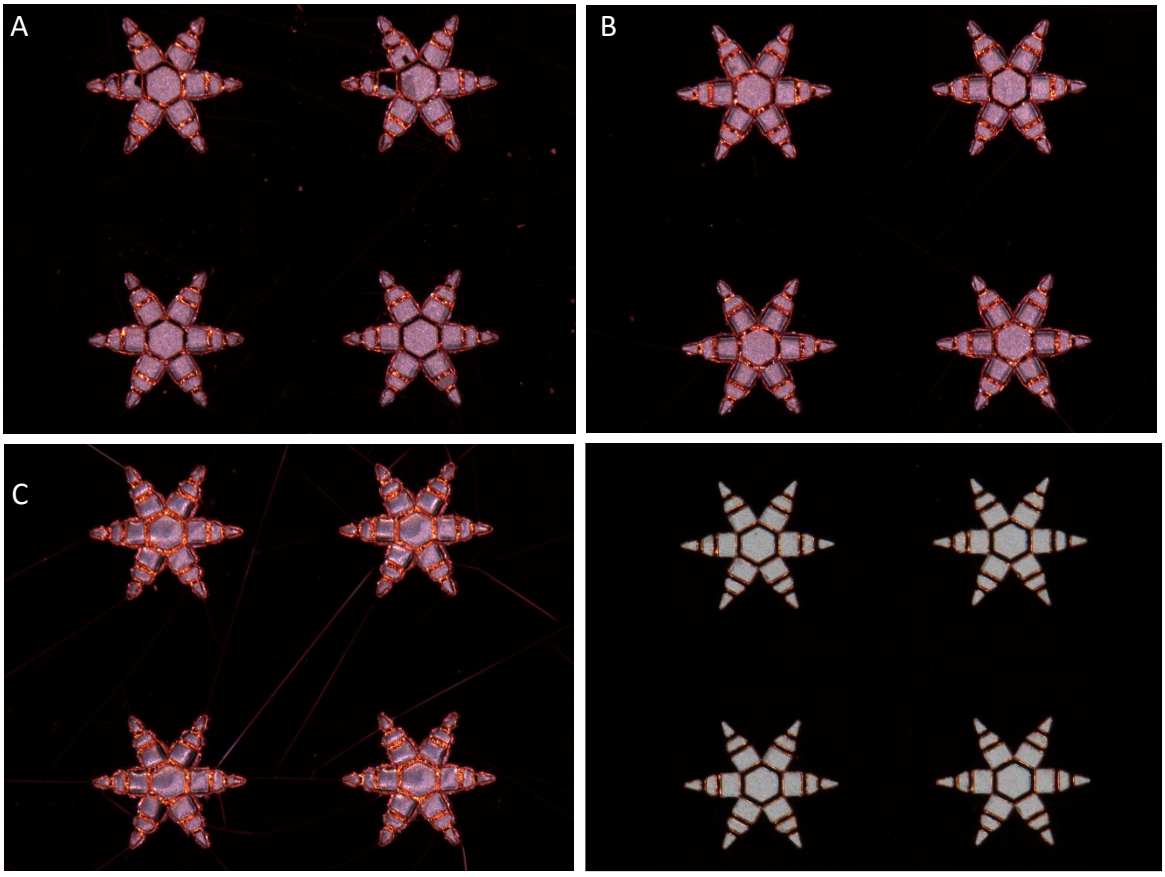

Figure 22: Effect of Current Density on Film Quality (Edges). (a) 10 mA/cm^2 (b) 20 mA/cm^2 (c) 30 mA/cm^2 (d) 40 mA/cm^2. Few of the grippers have uniform coating even at lower current densities. 40 mA/cm^2 displayed uniform coating throughout all the grippers

Since the mass of cobalt deposited onto the grippers are same at all four current densities, the grippers at lower current densities have a thicker coating on the edges of the wafers to make up for others with poor and insufficient coating. This phenomenon is known as the edge effect and is the result of electrons maximizing the distance from one another due to their repulsive behavior. As a consequence, the electric field is concentrated on the regions where the electrons are confined, such as the edges. Furthermore, due to the slow nucleation rate, regions that begin to nucleate earlier grow at the expense of others. To verify this, as shown in **table 3**, we measured the thickness of the grippers with uniform coating at varying current densities using a Dektak Surface Profilometer.

Table 3: Thickness of the Co grippers with uniform coating

Gripper sample	10 mA/cm^2	20 mA/cm^2	30 mA/cm^2	40 mA/cm^2
1	65.0 µm	26.7 µm	26.3 µm	8.87 µm
2	27.8 µm	30.4 µm	18.2 µm	8.74 µm
3	30.1 µm	31.3 µm	27.0 µm	8.35 µm
4	59.5 µm	37.2 µm	21.0 µm	7.91 µm
Average	45.6 ± 16.4 µm	31.4 ± 4.34 µm	23.12 ± 4.24 µm	8.47 ± 0.43 µm

From this table, we see that cobalt plating at a current density of 40 mA/cm^2 produces near uniform coating of our desired thickness, 8.5 µm; the grippers with uniform coating at lower current densities exceeded our desired thickness by a substantial amount. As the current density increases, the coating becomes more uniform. The higher overpotential caused by an increase in current density alleviates the nucleus process

energy and increases the nucleation rate [55]. Therefore, the grain size decreases and the surface becomes smoother. Extensive studies, SEM, and XRD have shown that this relationship holds true for most metals and alloys [52] [55] [56].

Based on the optical images, we found that a current density of 40 mA/cm^2 produced the highest film quality of cobalt. To examine the magnetic properties of the grippers, we measured he hysteresis loops of the grippers at 40 mA/cm^2 in plane field.

3.5.2 Magnetic Properties of the Electroplated Cobalt

Figure 23 shows the hysteresis loops of the cobalt and nickel microgrippers

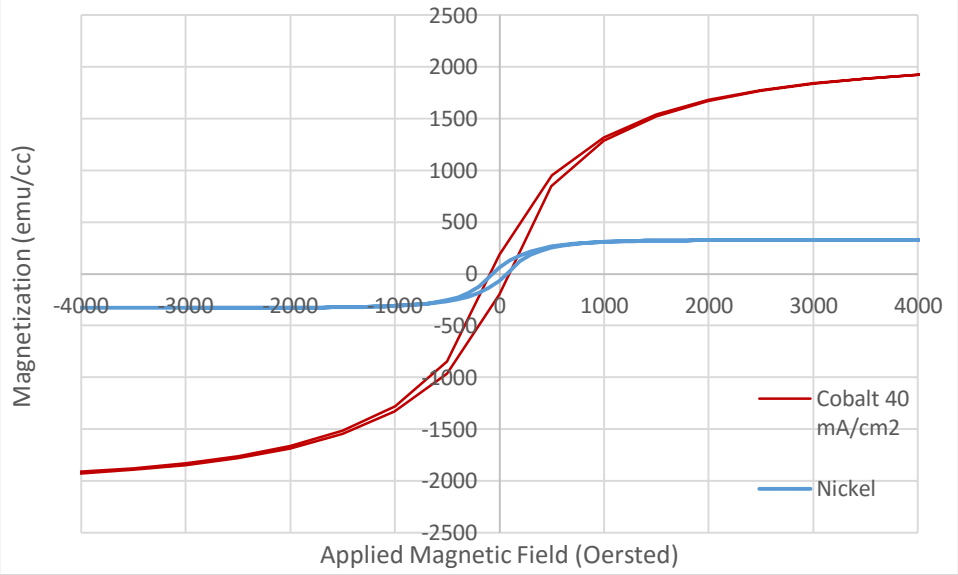

Figure 23: Hysteresis Loops of Co and Ni Microgrippers. Co microgrippers have a stronger overall magnetization

Although the shape of the Co gripper's hysteresis looks similar to that of Ni grippers, both x and y axis increased by almost two-fold. As previously mentioned, cobalt reaches magnetic saturation at a higher applied field strength due to its lower relative permeability. However, the substantial increase in the y-axis make up for the sizeable

field strength required to reach saturation induction. As shown in **Table 4**, the overall magnetization of cobalt grippers is higher than that of nickel grippers.

Table 4: Magnetic properties of nickel and cobalt microgrippers

Magnetic Properties	Nickel	Cobalt ($40\ mA/cm^2$)
Saturation Magnetization, M_s (emu/cc)	329	1921
Residual Magnetization, M_r (emu/cc)	64.5	184.3
Coercive Force (Oe)	72	89
Squareness M_r / M_s	.196	.096

From **Table 4**, we see that both saturation and residual magnetization increased immensely for cobalt grippers. Although we weren't able to achieve ideal squareness and large coercivity, the increase in the residual and saturation magnetization ensured that the magnetic properties of the grippers were optimized.

As shown in **figure 19**, we may have further increased the magnetic properties of the grippers and possibly obtained a square loop had we deposited cobalt alloys. However, this process brings forth two other variables that impact the magnetization of the grippers: the composition of the alloy, and the microstructures/ grain size of the coating. Comprehensive imaging links the relationship between the compositions of the cobalt alloy, their impact on the microstructures of the coating, and their effect on magnetism [46] [51]. In order to remove any bias that may have affected the results, we decided to electroplate pure single-phase cobalt.

Apart from potential fabrication mistakes, there is one main source of calculation error; we applied an external field with a step size of 500 Oe for Co grippers and 100 Oe for Ni grippers. Therefore, much of the values such as the residual magnetization and coercivity of the grippers were extracted from the data. Nevertheless, the increase in residual magnetization by 286% and saturation magnetization by 584% shows that the grippers can be more easily manipulated. To further characterize the grippers, we compared the two with respect to our collaborative work with the University of Twente.

3.5.3 Challenges in the Pac-Man Experiment

Our collaborators were unable to move the grippers due to the lack of force exerted by the electromagnets. The force exerted on a moving charge is defined by **equation 10** or the Lorentz Force Law [42]

$$\vec{F} = q\vec{v} * \vec{B} \qquad \text{[Equation 10]}$$

Where F is the force in Newton, q is the charge, v is the velocity in m/s, and B is the overall field in tesla.

Figure 24 shows the Lorentz Force visualized as an interaction between magnets, similar to our Pac-Man setup.

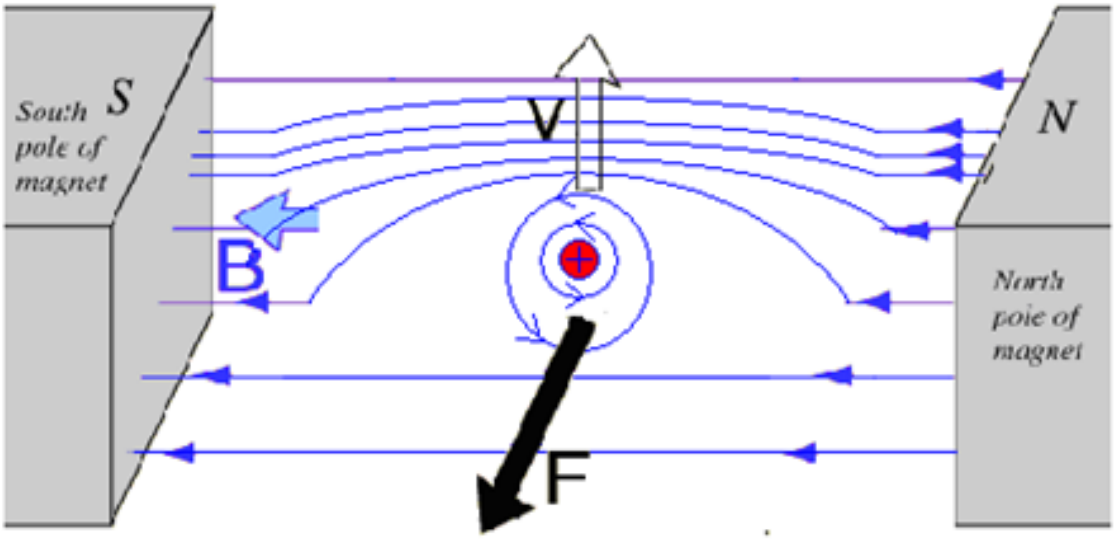

Figure 24: Interaction between Magnets. The vectors of the components can be demonstrated by the right hand rule. Copyright © 2012 Hyperphysics. Image reprinted with permission from Ref. [42]

Lorentz Force Law can also be manipulated to calculate the force exerted on a magnetic material, or our gripper by **equation 11** [58]

$$\vec{F} = V(M * \nabla)B = \mu_t * \nabla B \qquad \text{[Equation 11]}$$

Where F is the force in N, V is the volume of the material in cm^3, M is the magnetization of the material in emu/cm^3, B is the overall field in tesla, and μ_t is the net dipole moment in emu.

From here we see that the force exerted on the gripper is directly related to the net dipole moment at the applied field strength. Our collaborators informed us that they were applying a field of 150 Gauss, which corresponds to 150 Oe in a vacuum. We found that at 150 Oe, four Ni grippers produced .000793 emu, while four Co grippers at 40 mA/cm^2

produced .00278 emu. A net increase of 3.50 times is a significant improvement due to the amount of field gradient required to exert a force at microscale.

When the particles of a bulk material are created with dimensions in the micro/ nano scale, the properties of the material change drastically [49]. These include changes in the physical, chemical, electrical, mechanical, and optical properties [49]. The changes in these properties are due to two reasons: the effects of quantum mechanics and the increase in the surface area to volume ratio [49].

Since force exerted on a magnetic material is dependent on volume, the force becomes substantially smaller and the required field gets considerably larger at microscale [58]. Furthermore, since viscous drag forces from bodily fluids are dependent on the surface area, applications of these grippers and other bioMEMS pose a considerable challenge [58]. Therefore, the optimization of magnetic properties was vital for the development of microbotics and the applications of microgrippers in the human body.

Chapter 4. Applications in a Dynamic Environment

Advancements in micro and nanotechnology has enabled novel applications of bioMEMS to deliver drugs, perform diagnostic procedures, and repair tissues [58]. Their small size and stress-powered actuation make them ideal in various clinical settings. Microgrippers have the potential to improve existing minimally invasive procedures and enable new therapies. However, we must overcome multiple design challenges before these dust sized tools can navigate and perform life-altering procedures in our bodies.

First, they must be biocompatible. The design of our metallic grippers currently utilize a photoresist based trigger layer that is unsafe for the body. We looked into some other alternatives and found paraffin wax to be most promising due to its biocompatibility and body temperature melting point. However, further studies must be conducted on its properties before it can utilized as an improved trigger layer. Microgrippers must easily enter the body, navigate inside, operate, and leave the body in a noninvasive manner; these tasks are very challenging due to the dynamics of our circulatory system. We hope that the electroplating of cobalt will generate sufficient field to achieve these goals.

As technology improves, we can visualize surgical microgrippers carrying out complex tasks autonomously. The most envisioned application of microgrippers for surgery is material removal by mechanical means. Microgrippers have already shown their applications in several biopsies and their potential to cut through sturdy connective tissues. By repeating the procedure in minimally invasive surgery, they can be used to perform endoluminal tasks such as the removal of fatty acid deposits [59].

Another application for the microgrippers is drug delivery. The grippers can be coated with a biocompatible polymer consisting of the drug to conceal the therapeutic agents from the immune system and prolong its circulatory time by reducing renal clearance. Our lab has also studied the use of paraffin wax as a potential sustained drug delivery compartment and found favorable results. To make drug delivery a feasible application, we must look more into the specifics of the drug such as its pharmacodynamics and its compatibility with the materials used.

Although we can conceptualize the microgripper's improvements and novelties in medical technology, there is still a need for more testing and development. First on our agenda is the Pac-Man experiment; we hope that the improvement in the magnetization of the grippers will allow us to advance with this experiment and take it a step further as an autonomous surgical tool. Next, we plan to measure the gripping force of these devices to quantify their mechanical strengths. We are currently collaborating with the University of Twente on both experiments and hope to eventually develop the microgrippers into a viable surgery and drug delivery tool.

Chapter 5. Conclusion

Through a series of microfabrication steps, we created dust sized grasping tools on a silicon wafer. Due to their polymeric trigger layer and metallic panels, they respond to both temperature and magnetic field. Furthermore, their parallel production and wireless actuation provide distinct advantages over current surgical instruments. These grippers have already shown their potential in multiple biopsies procedures, where they increased the efficiency and minimized the risk of tissue damage.

However, they have yet to perform tasks autonomously in the human body. One of the main challenges is the need for a strong magnetic material that can guide the gripper in a cluttered and dynamic environment. Due to the increased surface area to volume ratio at microscale, the field required to exert force on the grippers and the viscous drag forces opposing the grippers becomes increasing large. Therefore, the optimization of the magnetic properties is essential to move forward with this technology.

In order to further the concepts presented in this thesis, we plan to collaborate with the robotics lab to perform pick and place tasks autonomously in a dynamic environment. If the experiments are successful, the microgrippers may very well revolutionize minimally invasive surgery and drug delivery.

References

1. Jaffray, B. (2005). Minimally invasive surgery. *Archives of disease in childhood*, *90*(5), 537-542.
2. Geis, W. P. (2004). J. Barry McKernan, MD, PhD—A Profile. *JSLS : Journal of the Society of Laparoendoscopic Surgeons*, *8*(4), 399–400.
3. Cholecystectomy. (2012). *Drugline*. Retrieved from http://drugline.org/medic/term/cholecystectomy/
4. Robinson, T., & Stiegmann, G. (2007). Minimally invasive surgery. *Endoscopy, 39*(1), 21-23.
5. Peters, W., Jr. (2013). Minimally Invasive Surgery Expanded Version. *ASCRS*.
6. Laparoscopic Instruments for Minimally Invasive Surgeries: Access & Exposure Equipment vs. Surgical Instruments. (2016). Retrieved April 02, 2016, from http://medinstrum.com/laparoscopic-instruments/
7. Talamini, M. (2013). Point-Counterpoint: Are there significant advantages for robotic vs. laparoscopic surgery for abdominal procedures? *ACS Surgery News*.
8. Wright, JD (2015). Comparative Effectiveness of Robotically Assisted Compared With Laparoscopic Adnexal Surgery for Benign Gynecologic Disease. *Obstetrical & Gynecological Survey, 70*(2), 83-85.
9. Da Vinci Si System. (2016). *Intuitive Surgical Inc.*, Retrieved from http://www.intuitivesurgical.com/company/media/images/systems-si/da_Vinci_action_023874_10x7_150dpi.jpg
10. Fuchs, K. H. (2002). Minimally Invasive Surgery. *Endoscopy, 34*(2), 154-159.

11. Watson, DI, Baigrie, RJ, Jamieson, GG. A learning curve for laparoscopic fundoplication. Ann Surg 1996;224:198–203
12. Barbash, G. I., Glied, S. A. (2010). New Technology and Health Care Costs — The Case of Robot-Assisted Surgery. *New England Journal of Medicine N Engl J Med, 363*(8), 701-704.
13. Zimmermann, B. K. (2015). Circulatory System: Facts, Function & Diseases. *livescience*
14. Topol EJ. Cleveland Clinic Heart Book (2000) New York: Hyperion
15. Taylor, T. (2009). Cardiovascular System. *Innerbody*.
16. Marieb, E. N., Hoehn, K., Hutchinson, M. (2013). *Human anatomy & physiology*. San Francisco, Calif.: Pearson Education/Benjamin Cummings.
17. Blakemore, C., Jennett, S. (2001) "blood vessels." *The Oxford Companion to the Body*.
18. Lichtin, A. Components of Blood. *Merck Manual*.
19. Eastcott, H. H. G. (1981), Gray's Anatomy. Edited by P. L. Williams and R. Warwick. Thirty-sixth edition.
20. Bowers, N. (2009). What Are White Blood Cells? *University of Rochester Medical Center*.
21. Bergman, R. Atlas of Microscopic Anatomy: Blood. *Anatomy Atlases*.
22. Platelet Disorders. (2008). *NIH: National Heart, Lung, and Blood Institute*.
23. Human Anatomy: Blood - Cells, Plasma, Circulation, and More. (2014). *WebMD*. Retrieved from http://www.webmd.com/heart/anatomy-picture-of-blood

24. Fernandes, R., Gracias, D. H. (2009). Toward a miniaturized mechanical surgeon. *Materials Today, 12*(10), 14-20.
25. Lawrence TS, Ten Haken RK, Giaccia A. (2008). Principles of Radiation Oncology. Cancer: Principles and Practice of Oncology. 8thed.
26. Feynman, R. P., *J.* (1992) *Microelectromech.* 1, 60.
27. Leong, T. G., Randall, C. L., Benson, B. R., Bassik, N., Stern, G. M., & Gracias, D. H. (2009). Tetherless thermobiochemically actuated microgrippers. *Proceedings of the National Academy of Sciences, 106*(3), 703-708.
28. Gultepe, E., Randhawa, J. S., Kadam, S., Yamanaka, S., Selaru, F. M., Shin, E. J., Gracias, D. H. (2012). Biopsy with Thermally-Responsive Untethered Microtools. *Adv. Mater. Advanced Materials, 25*(4), 514-519.
29. Mijatovic, D., Eijkel, J. C., & Berg, A. V. (2005). Technologies for nanofluidic systems: Top-down vs. bottom-up—a review. *Lab on a Chip Lab Chip, 5*(5), 492.
30. Zangari, G. (2010) Microelectromechanical Systems, in Modern Electroplating, Fifth Edition, John Wiley & Sons, Inc., Hoboken, NJ, USA. doi: 10.1002/9780470602638.ch28
31. P. Andncacos and L. Romankiw, "Magnetically soft materials in data storage: their properties and electrochemistry'," IBM Research Division, Thomas J. Watson Research Center, Yorktown Heights, New York 10598, pp. 227-321
32. Dufour, J. (2006) *An Introduction to Metallurgy*, 5th ed. IX-1.
33. Mack, C. A. (2006) Field Guide to Optical Lithography, *SPIE Press*, Bellingham, WA.

34. Shea, J. (2002). Handbook of thin film deposition - processes and technologies, 2nd edition [Book Review]. *IEEE Electrical Insulation Magazine IEEE Electr. Insul. Mag., 18*(4), 47-47.

35. Kumar, S., Pande, S., & Verma, P. (2015). Factor Effecting Electro-Deposition Process. *IJCET*.

36. Jaeger, Richard C. (2002). "Film Deposition". *Introduction to Microelectronic Fabrication* (2nd ed.). Upper Saddle River: Prentice Hall.

37. Prakash, A. (2013). A Review of various Wet Etching Techniques used in Micro Fabrication for Real Estate Consumption. *International Journal of Computer Applications*.

38. Nayak, A., Logeeswaran V.J., Islam, M. (2012) Wet and Dry Etching. *Encyclopedia of Nanotechnology*

39. Whyte, W. (2001). *Cleanroom technology: Fundamentals of design, testing, and operation*. Chichester: J. Wiley.

40. Pandey, S., Gultepe, E., & Gracias, D. H. (2013). Origami Inspired Self-assembly of Patterned and Reconfigurable Particles. *Journal of Visualized Experiments : JoVE*, (72), 50022. Advance online publication. http://doi.org/10.3791/50022

41. ferromagnetism. (2016). In *Encyclopædia Britannica*.

42. Nave, R. (2012). Electricity and Magnetism. *HyperPhysics*.

43. Sung, H., & Rudowicz, C. (2002). A closer look at the hysteresis loop for ferromagnets. *ArXiv*.

44. Anhalt, J., Crowell, B., Crunkilton, D., & Kuphaldt, T. (n.d.). Permeability and Saturation. *AAC Volume 1*. Retrieved from

http://www.allaboutcircuits.com/textbook/direct-current/chpt-14/permeability-and-saturation/

45. Cobalt Facts. (2006). *CDI*.

46. Myung, N. V., Park, D., Yoo, B., & Sumodjo, P. T. (2003). Development of electroplated magnetic materials for MEMS. *Journal of Magnetism and Magnetic Materials, 265*(2), 189-198. doi:10.1016/s0304-8853(03)00264-6

47. B-H Curve (2013). vlab.amrita.edu. Retrieved from vlab.amrita.edu/?sub=1&brch=282&sim=1507&cnt=1

48. Bradley, K. (2011). Nickel Applications & Uses. *NiPERA*.

49. Nanotechnology 101: What's so special about the nanoscale? (2011). *NNI*.

50. Liao, S.H. (1998). IEEE Trans. *Magn*. 23 2981.

51. Armyanov, S. (2000). Crystallographic structure and magnetic properties of electrodeposited cobalt and cobalt alloys. *Electrochimica Acta, 45*(20), 3323-3335. doi:10.1016/s0013-4686(00)00408-4

52. Haerifar, M., & Zandrahimi, M. (2013). Effect of current density and electrolyte pH on microstructure of Mn–Cu electroplated coatings. *Applied Surface Science,284*, 126-132. doi:10.1016/j.apsusc.2013.07.049

53. Tuaweri, T., Adigio, E., & Jombo, P. (2013). A Study of Process Parameters for Zinc Electrodeposition from a Sulphate Bath. *IJESI*.

54. Chen, W. (2007). *The VLSI handbook*. Boca Raton, FL: CRC/Taylor & Francis.

55. Shahri, Z., & Allahkaram, S. (2011). Effect of particles concentration and current density on the cobalt/hexagonal boron nitride nano-composite coatings properties. *Iranian Journal of Materials Science and Engineering*.

56. Gómez, E., & Vallés, E. (2002). Thick cobalt coatings obtained by electrodeposition. *Journal of Applied Electrochemistry*.

57. Adeli, B., Sohi, M. H., & Mehrizi, S. (2012). Effects Of Sodium Citrate And Current Density On Electroplated Nanocrystalline Cobalt-Iron Thin Films. *International Journal of Modern Physics: Conference Series Int. J. Mod. Phys. Conf. Ser., 05*, 696-703. doi:10.1142/s201019451200264

58. Nelson, B. (2006). Microrobotics in Medicine. *JNRR*.

59. Nelson, B., Kaliakatsos, I., & Abbott, J. (2010). Microrobots for Minimally Invasive Medicine. *Annual Reviews*.

Curriculum Vitae

Hyun Soo Yoon

115 W 29th Street Baltimore, MD 21218
562-298-7869 | hyoon26@jhu.edu

EDUCATION

Johns Hopkins University Baltimore, MD
Master of Science in Chemical and Biomolecular Engineering May 2016
Thesis**:** *Surgical Microgrippers and Their Applications in a Dynamic Environment*
Related Coursework: Micro/Nanotechnology, Interfacial Science with Applications to Nanoscale Systems, Nanobioengineering Lab, Supramolecular Materials/ Nanomedicine, Advanced Thermodynamics/Kinetics

Johns Hopkins University Baltimore, MD
Bachelor of Science in Chemical and Biomolecular Engineering May 2015
Concentration: Interfaces and Nanotechnology
Overall GPA: 3.33
Related Coursework: Chemical Process/Product Design, Modeling Dynamic/Control, Polymer Chemistry/Physics

SKILLS

Technical: Photolithography, Soft Lithography, Vapor Deposition, Electrodeposition, Dry/Wet Etching, Optical/ Electron Microscopy, Nanoparticle Synthesis, Cell Culture, Clean Room Protocol
Software: MATLAB/Simulink, AutoCAD, ASPEN, Adobe Illustrator, Microsoft Office

EXPERIENCE

Gracias Nanotechnology Lab
Baltimore, MD
Research assistant
September 2012 - present

- Fabricate submillimeter star shaped devices that can travel through natural orifices in the body and perform biopsies through self-folding
- Utilize microfabrication techniques in a clean room setting to pattern metals and polymers into surgical devices that respond to thermal and magnetic cues
- Train two undergraduate students in photolithography and thin film deposition on silicon wafer substrates
- Optimize the grippers by exploiting different materials and developing techniques for fabrication

PROJECTS

Surgical Microgrippers and Their Applications in a Dynamic Environment
Master's Thesis June 2015 – May 2016

- Collaborate with the University of Twente to precisely control the microgrippers in a cluttered setting to perform pick and place tasks through electromagnets and image based control
- Optimize the grippers by exploiting different materials and developing techniques for fabrication

Microwells for HEK293 Cell Culture and Analyses
Nanobioengineering Lab Jan 2016 – May 2016

- Design the photomasks using AutoCAD and fabricate microwells for HEK293 cell culture using PDMS soft lithography
- Test the morphology of the cell in exposure to different nanoparticles and characterize them using optical and electron microscopy

Production of Acrolein from the Catalytic Oxidation of Propene
Senior Process Design Jan 2015 – May 2015

- Diagram a grass roots facility that produces 40,000 metric tons/year of 99 wt% acrolein from catalytic gas phase oxidation of propene
- Design the process and model the process flow in ASPEN using a fluidized bed reactor and several separation columns/ recycle streams